

**THIS DOCUMENT IS PART OF A NEW BOOK, IT IS BROUGHT TO YOU FREELY BY THE OPEN ACCESS JOURNAL MATERIALS AND DEVICES**

Publication date: 2021, january 14th

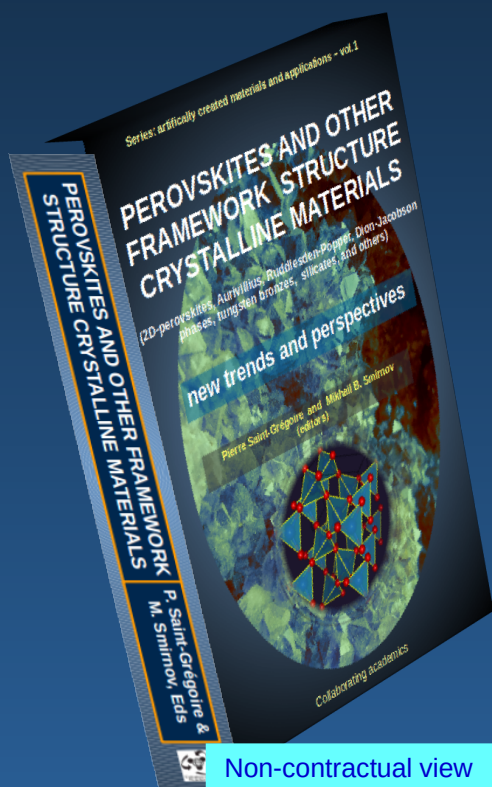
The book,  
**“PEROVSKITES AND OTHER FRAMEWORK  
STRUCTURE MATERIALS**

(2D-perovskites, Aurivillius, Ruddlesden-Popper, Dion-Jacobson phases, tungsten bronzes, clays, and others)

**New trends and perspectives”**

(editors P. Saint-Grégoire and M.B Smirnov)

Is a collective volume of 800 pages with **76 authors** and **26 chapters** on recent developments and hot subjects, divided into two parts:



**A. Fundamental aspects and general properties**

**B. Elaborated materials and applied properties**

Available in 3 formats:

- Ebook
- printed softcover, black & white
- printed hardcover, color.



**Go to the Book(click)**

Non-contractual view

---

## Chap. 2 : Functional Perovskites: Structure-Properties Correlations

---

A. K. Bera (1) and S. M. Yusuf (1,2)

(1) Solid State Physics Division, Bhabha Atomic Research Centre,  
Mumbai 400085, India

(2) Homi Bhabha National Institute, Anushaktinagar, Mumbai 400094,  
India

**Corresponding author:** smyusuf@barc.gov.in

**Abstract:** The perovskite structure with general formula  $ABX_3$  shows its multidimensional nature in regards to correlations of crystal structures with electronic, magnetic, optical, and catalytic properties. Perovskites are utilized in a large range of applications due to their tremendous versatility. In this chapter, structure-properties correlations in oxide perovskite compounds  $ABO_3$  having several functional properties are presented. In particular, neutron and x-ray diffraction results are described to reveal a direct correlation of several important physical properties, such as magnetic, multiferroic, electronic (CMR), and SOFC electrodes with the crystal structures.

**Keywords:** REVIEW PEROVSKITES, FUNCTIONAL PEROVSKITES, CRYSTAL STRUCTURE, MAGNETIC STRUCTURE, NEUTRON DIFFRACTION

<b>Cite this paper:</b> A.K. Bera and S. M. Yusuf, OAJ Materials and Devices, vol 5(1), Chap No 2 in “Perovskites and other Framework Structure Crystalline Materials”, p39 (Coll. Acad. 2021) DOI:10.23647/ca.md20202105
--

## I. Introduction

---

Perovskites with the formula  $ABX_3$ , where  $A$  and  $B$  are metal ions and  $X$  is oxygen (or other large ions, such as fluorine, chlorine, bromine, and iodine), form one of the most studied structural families in the solid-state chemistry, physics, and material sciences. Perovskite (the mineral calcium titanate  $\text{CaTiO}_3$ ) was discovered by Gustav Rose in 1839 and it was named after the Russian mineralogist Lev Perovski. The crystal structure of perovskite was first published in 1926 by Goldschmidt (1). Since then, perovskites remain one of the central interests of research due to an enormous flexibility of the crystal structure to accommodate a large number of cations (both at the  $A$  and  $B$  sites), to tolerate distortions, and to accommodate non-stoichiometry, as well as for their fascinating structure-property correlations with a wide variety of physical and chemical properties, such as magnetic, multiferroic, superconductivity, ionic conductivity, piezoelectricity, colossal magnetoresistance, optical, photoluminescence, and catalytic. The above spectrum of properties arises from a complex interplay between spin, charge, orbital, and lattice degrees of freedoms. In the perovskite structure, the  $A$  cation can be mono, di, or trivalent, whereas  $B$  cation can be a di, tri, tetra, penta or hexa-valent. The flexibility on the choice of  $A$  and  $B$  ions gives an enormous possibility for partial or total ionic substitutions which result into an incredibly large number of compounds with diverse physical and chemical properties depending on the (i) oxidation states and nature of cations, (ii) stoichiometry of anions and cations and (iii) the nature of crystal structure.

The present chapter on perovskite materials comprises the details of the fundamental properties and their link to the underlying crystal structure. As the crystal structure of perovskite is the backbone of the spectrum of physical properties, we trace on the structure-properties correlations in the present chapter. The rich and versatile crystal structures of perovskites have been investigated by several experimental techniques. In this regard, diffraction experiments, especially neutron diffraction play the main role (2). Besides, neutron diffraction provides the microscopic nature of the magnetic ground states and their dependence on the temperature, magnetic field, pressure, etc. In the current chapter, we emphasize the role of neutron diffraction to investigate and understand the rich physics of perovskites. This chapter spans over eight sections. In the next section (section # II), we cover the general aspects of crystal-structural and physical properties of perovskites, as well as the fundamental origin of such physical properties. In particular, this section includes examples of crystal structural phase transitions and distortions, electronic structures under crystalline electric fields, magnetic interactions, multiferroic properties, and colossal

magneto-resistance (CMR) properties. This section also covers properties of nano-structured perovskites, strain and interfacial effects in thin films of perovskites, applications of perovskites, as well as preparation methods of perovskites. The sections III, IV, V, and VI are designed on the specific physical properties as follows:

- *the magnetic properties of perovskites and their correlations with the crystal structure*—the effects of cation order/disorder, doping, structural distortion on the magnetic properties, and their use for tuning and optimizing magnetic properties;
- *the multiferroic properties of perovskites*—experimental progress, correlations to the crystal structure, and underlying physics;
- *the electronic properties of perovskites*—CMR effect in perovskite manganites and its effective tuning via the choice of trivalent rare-earth ions  $T$  and divalent alkali metal ions  $D$  elements at the  $A$ -site of  $AMnO_3$  perovskites.
- *perovskites for solid oxide fuel cell (SOFC) applications* — the stable crystal structure over the operating high temperatures, and high ionic conductivity.

In section VII, we give an overview of the future prospective in the area of versatile perovskites, followed by a concluding section.

## II. Basic Properties of Perovskites

---

### II.1 Crystal structure, distortion, and phase transitions

The ideal perovskite  $ABO_3$  crystal structure is cubic with space group  $P-3m3$ , where the  $A$  atoms occupy at the cube corner positions  $(0, 0, 0)$ ,  $B$  atoms occupy at the body-center position  $(1/2, 1/2, 1/2)$ , and oxygen atoms occupy the face center positions  $(1/2, 1/2, 0)$  (Fig. 1). In this crystal structure, the  $B$  cations sit in a 6-fold coordination, surrounded by an octahedron of oxygen atoms, and the  $A$  cation sits in a 12-fold cuboctahedral coordination. The stability of the cubic structure is quite stringent and strongly depends on the relative ionic sizes of  $A$ ,  $B$ , and  $O$  atoms. In the idealized cubic perovskite structure, the radii of the ions can then be related to

$$R_A + R_O = \sqrt{2}(R_B + R_O) \quad (1)$$

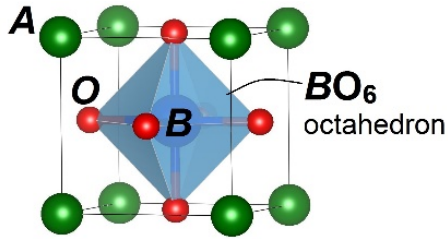


**Figure 1:** Ideal (Cubic) perovskite crystal structure. Cation B is surrounded by six oxygen ions in an octahedral configuration. A site is surrounded by 12 oxygen ions (not shown).

where,  $R_A$ ,  $R_B$ , and  $R_O$  are the relative ionic radii of the A and B site cations and the oxygen ion, respectively.

A deviation from the ideal cubic structure may occur due to non-ideal atomic radii ratios, or electronic and magnetic effects. With decreasing the size of A cation, beyond a certain point, the cations would be too small to remain in contact with the anions in the cubic structure. Therefore, to keep the contact, the B-O-B angle bends from its ideal value of  $180^\circ$  and results in a tilting of the  $BO_6$  octahedra. Such distortion could be accounted by an introduction of a constant,  $t$ , in Eq. 1

$$R_A + R_O = t\sqrt{2}(R_B + R_O) \quad (2)$$

The constant,  $t$ , is known as the Goldschmidt's tolerance factor and can be used as a measure of the degree of distortion of a perovskite with respect to the ideal cubic crystal structure which occurs for  $0.89 < t < 1$  (4). A slight buckling and distortion of octahedra can produce several lower-symmetry distorted crystal structures.

With the decreasing tolerance factor (either by the decrease of the A cation radius and/or by the increase of the B cation radius) the octahedra tilting leads to a distorted orthorhombic structure with space group  $Pnma$  for  $0.75 < t < 0.89$ . The distorted orthorhombic structure is shown in Fig. 2(a). The unit cell of the distorted orthorhombic structure is double in size than that of the cubic cell, and has two nonequivalent oxygen positions in the unit cell. Further distortion of the perovskite structure can result in a rhombohedral crystal structure with the space group  $R-3c$  [Fig. 2(b)]. The largest deviations ( $t < 0.75$ ) lead to a structure with a hexagonal  $P6_3cm$  crystal symmetry [Fig. 2(c)]. In the hexagonal structure, the lattice distortions are so large that the A cations have a 7-fold coordination and the B cations have a 5-fold coordination, and the structure loses its direct similarity with the perovskite symmetry.

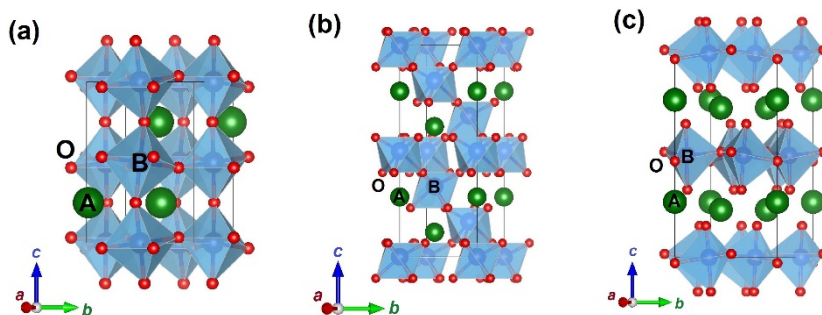


**Figure 2:** The distorted  $ABO_3$  perovskite crystal structures with (a) orthorhombic (space group:  $Pbnm$ ), (b) rhombohedral (space group  $R3c$ ), and (c) hexagonal (space group:  $P6_3cm$ ) symmetry.

Theoretical calculations for perovskites using the group-theoretical method establish 261 ordered low-symmetry structures with unique space-group symmetry (3). The space group relationships associated with particular tilt systems for  $ABO_3$  perovskites identify possible first and second-order phase transitions from the primary cubic structure (4). Such kinds of different crystal structures have also been realized in a single compound with the variation of temperature; for example,  $BaTiO_3$  has four crystallographic phase transitions with decreasing temperature: cubic ( $Pm-3m$ ) to tetragonal ( $P4mm$ ) at 120 °C to orthorhombic ( $Amm2$ ) at 5 °C and then to rhombohedral ( $R-3m$ ) at -90 °C. Moreover, the perovskite structure could be further complex when it contains two different cations at the  $B$ -site. This results in the possibility of site ordered, site disordered variant crystal structures, and multi-functional physical properties (5-7).

## II.2 Electronic structures of transition metal perovskites

Perovskites having transition metal ions at the  $B$  site show a large variety of fascinating electronic and magnetic properties (8). The magnetism and electronic correlations usually originate from the unfilled  $3d$  electron shells of the transition metal ions, whereas, the dielectric properties are generally connected to the completely filled  $3d$  electron shells. The electronic correlations of such  $3d$  states are usually strong and localized, and determined by the larger ratio ( $U_d/W$ ) between the Coulomb repulsion energy  $U_d$  and the bandwidth  $W$ , that leads to a tendency for insulating states or a metal-insulator transition. The perovskite oxides serve as an important playground for

magnetism where unique properties and phenomena can be observed as a result of a close correlation among magnetism, orbital ordering, and lattice distortion (2, 3). The resultant properties of a compound are dictated by its electronic structure, *i.e.* the number of 3*d* electrons, the Hund's coupling, the crystalline electric field, or Jahn-Teller splitting of the 3*d* electron states by the surrounding ligand ions, and exchange couplings. A schematic representation of the energy level schemes for the 3*d* ions in the tetrahedral, octahedral, and square planar environments is shown in Fig. 3.

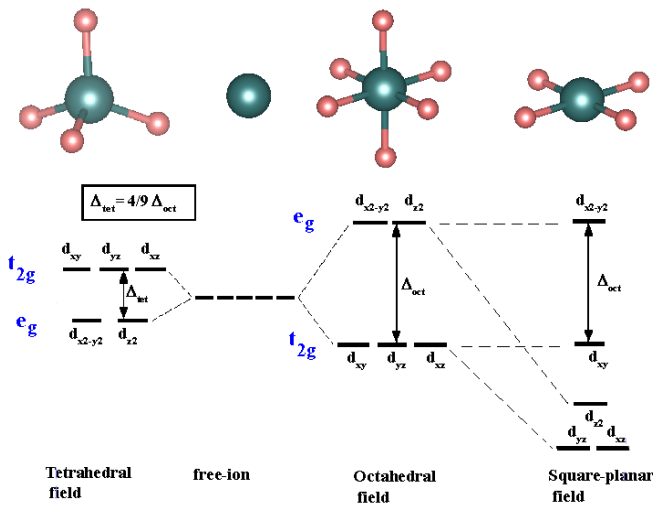


**Figure 3:** Crystal field splitting of 3*d* orbitals in the tetrahedral, octahedral, and square planar environment. (<http://wwwchem.uwimona.edu.jm/courses/CFT.html>.)

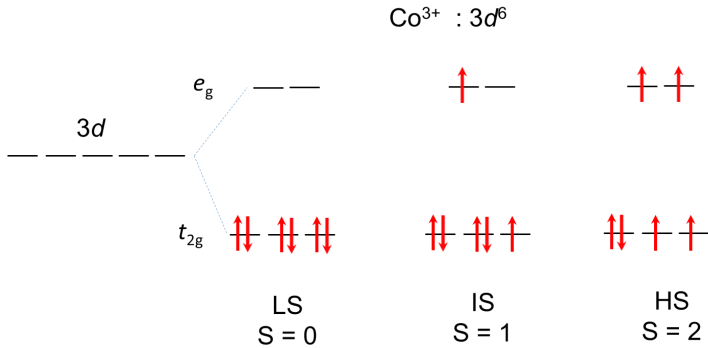


**Figure 4:** The low spin (LS), intermediate spin (IS), and high spin (HS) electron configurations for  $3d^6 \text{Co}^{3+}$  ion, as found in the perovskite compound  $\text{LaCoO}_3$ .

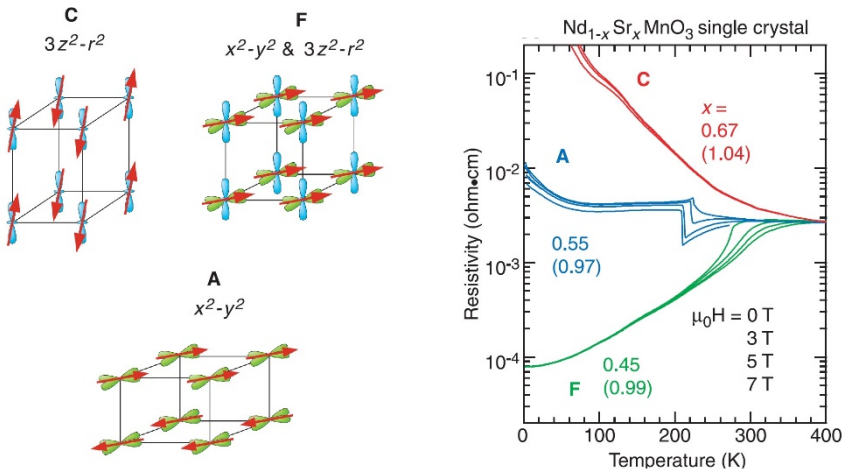


**Figure 5:** Left: The orbital and spin orders in the hole-doped manganite perovskite oxides  $\text{Nd}_{1-x}\text{Sr}_x\text{MnO}_3$ . C: chain type antiferromagnet, F: ferromagnetic-metallic, and A: 2D layered-type antiferromagnet with metallic state. Right: Temperature-dependent resistivity curves of  $\text{Nd}_{1-x}\text{Sr}_x\text{MnO}_3$  in various magnetic fields for the respective three magnetic phases (F, A, and C). The numbers in parentheses represent the  $c/a$  ratio (represent the uniaxial lattice strains) indicating the coupling of the magnetism to the orbital order (as shown in the left panel). (Reproduced with permission from Tokura *et al.*, Science, 288, 462 (2000). Copyright 2000 by the American Association for the Advancement of Science.)

The final spin configuration and effective total spin value depend on the relative strengths of the crystal field splitting energy and spin pairing energy. The various possible spin values for the  $\text{Co}^{3+}$  ion ( $3d^6$ ) in the octahedral crystal field are shown in Fig. 4. If the crystal field splitting energy is larger than the pairing energy, a low-spin (LS) state of  $\text{Co}^{3+}$  occurs where the total spin value  $S=0$ . If the crystal field energy is lower than the pairing energy, a high spin (HS) state configuration occurs and it results into a spin value of  $S=2$ . An intermediate spin state for  $\text{Co}^{3+}$  with spin value  $S=1$  is also possible. Moreover, in some cases, the spin crossover/transition between the LS state to the HS state may be induced by a change of temperature, pressure, or irradiation by light. The spin state transitions are found in the Co and V based perovskites (9). Due to the strong electron correlations in the transition-metal perovskite oxides, the couplings and interplays of the orbital and spin degrees of freedoms give rise to various electronic structures and novel phenomena including finite orbital moment, orbital ordering, metal-insulator transitions, high-temperature superconductivity, and colossal magnetoresistance (10). The representational orbital and magnetic orderings, as well as metal-insulating transitions in hole-doped manganite perovskite oxides are shown in Fig. 5.

We add here that an interesting situation arises when the  $B$  site is occupied by a nonmagnetic ion, and the  $A$  site is occupied by a rare earth ion, such as in the  $L(\text{Ga/Al})\text{O}_3$ , ( $L$  = rare-earth ions) compounds. Such compounds reveal interesting crystal-structural phase transitions which are attributed due to an interaction between the crystal vibrations and the electronic excitations of the  $L^{3+}$  ions. These materials have also substantial applications as substrate materials for growing thin films of high-temperature superconductors, magnetoresistive devices, GaN two-dimensional structure, etc.

Furthermore, the divalent alkali metal doped compounds (viz.,  $L_{1-x}A_x\text{Ga}_{1-y}\text{Mg}_y\text{O}_{3-\delta}$  and  $L_{1-x}A_x(\text{Mn/Co})\text{O}_{3-\delta}$ ) are promising materials for solid oxide fuel cells. The crystal electric fields (CEP) on the rare-earth  $A$ -site having a low-symmetry environment determine the thermodynamic and magnetic properties viz., the Schottky anomaly of the specific heat, electronic structure, and the anisotropy of the magnetic susceptibility as well as the various structural and magnetic phase transitions.

### II.3 Magnetic interactions in perovskite

The perovskite structure allows several magnetic exchange interactions including the superexchange interactions (both ferromagnetic (FM) and antiferromagnetic (AFM) types) between localized spins, and the ferromagnetic double exchange interactions

(11, 12) due to hopping of electronic charge carriers. The superexchange interaction occurs through a virtual transfer of the electron between two magnetic ions via the intermediate oxygen ions and can be an FM or an AFM type. The sign and strength of the superexchange interactions depend on the orbital configuration following the rules of Goodenough–Kanamori (Fig. 6).

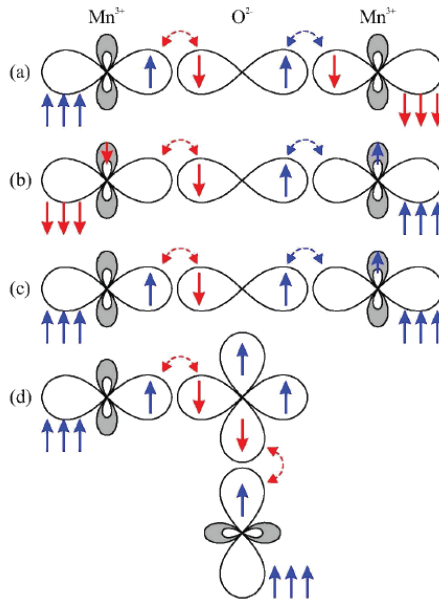


**Figure 6:** Antiferromagnetic [(a) and (b)] and ferromagnetic [(c) and (d)] types superexchange interactions between two  $\text{Mn}^{3+}$  ions defined by the Goodenough-Kanamori-Anderson rules. The  $d_{x^2-y^2}$  (shaded) and the  $d_{z^2}$  orbitals (to the left and right), as well as the  $p_z$  orbitals in the center of an Mn-O-Mn bond, are schematically illustrated. The three arrows outside the orbital denote the total core spin  $S = 3/2$  of the three (not shown)  $t_{2g}$  orbitals.

On the other hand, the FM double exchange interaction arises from a band broadening due to hybridization (13). In this case, a physical transfer of electron occurs between two magnetic sites and results in an FM metallic state (Fig. 7). Besides the superexchange and the double exchange interactions, an anisotropic exchange interaction, known as- the Dzyaloshinsky-Moriya (DM) interaction (14, 15), may also be present in perovskites. The DM interaction, mediated through the spin-orbit coupling, occurs when there is a lack of an inversion symmetry with respect to the center between the two interacting magnetic ions. The DM interaction  $H_{\text{DM}} = D_{12} \cdot [S_1 \times S_2]$  tries to force the two interacting spins  $S_1$  and  $S_2$  to make a right angle between

them, resulting in a spin canting of the magnetic moments (Fig. 8). The DM interaction is thus a source of a weak ferromagnetic behavior in an antiferromagnet. The DM interaction is responsible for the multiferroic behaviours in orthorhombic perovskites (16).

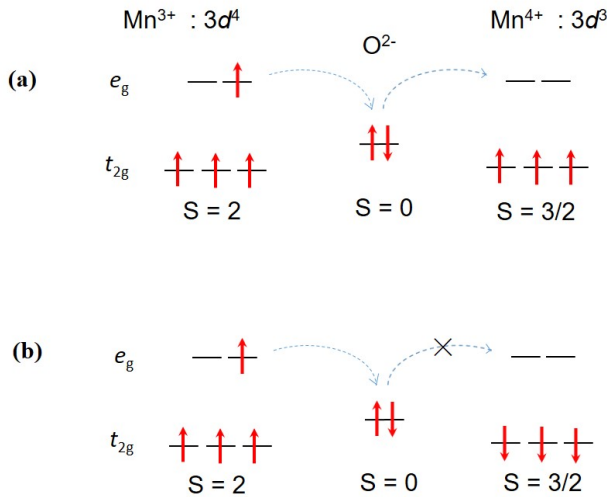


**Figure 7:** A schematic picture for the double exchange interaction favoring an FM coupling between the Mn ions mediated through an oxygen ion. The dashed connecting curves show the simultaneous charge transfer between the Mn and O atoms. The hopping occurs if (a) the neighboring ions are ferromagnetically aligned, and hopping does not occur if (b) the neighboring ions are antiferromagnetically aligned.

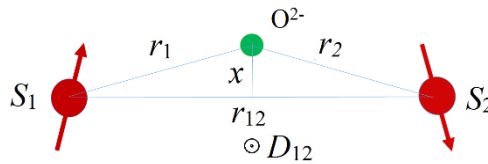


**Figure 8:** A schematic picture for Dzyaloshinsky-Moriya interaction. The Dzyaloshinskii vector  $D_{12}$  is proportional to spin-orbit coupling constant, and depends on the position of the oxygen ion.

The competing exchange interactions combined with the lattice and orbital degrees of freedom result in a multiplicity of the magnetic ground states and lead to a variety of magnetic ground states including FM, AFM, ferrimagnetic, spin-glass, etc. The perovskites with such exchange interactions allow experimental investigations of numerous fundamental magnetic states, including, the order of phase transition (17, 18) and long-range and/or short-range magnetic ordering (19). Such perovskites also allow one to realize quantum criticality (20), Griffiths phase, and exchange bias (21-23) phenomena.

## II.4 Multiferroicity in perovskites

Perovskites are versatile and provide an experimental realization of the rare phenomenon of multiferroic; a coexistence of more than one primary ferroic order parameter i.e., ferromagnetism, ferroelectricity, and ferroelasticity in a material (16, 24, 25). Multiferroics with spontaneous magnetization and electric polarization are promising candidates for advanced energy-efficient memory devices with faster speeds. According to the Khomskii's classification (26), there are two types of multiferroic materials; (i) type-II multiferroics (or so-called magnetic multiferroics), in which the origin of ferroelectric polarization is due to magnetic ordering, and (ii) type-I multiferroics where the origin of polarization is nearly irrelevant of magnetism. The rare-earth manganite  $RMnO_3$  perovskites reveal both type-I and type-II multiferroics (27). The type-II multiferroic  $RMnO_3$  compounds exhibit strong intrinsic magnetoelectric couplings, which means that the ferroelectric polarization is tunable by magnetism, while in most type-I multiferroic  $RMnO_3$  compounds, the magnetoelectric coupling is usually weak.

## II.5 Colossal magnetoresistance in perovskites

The perovskites, furthermore, yield the realization of colossal magnetoresistance (CMR), a property that arises mostly from the manganese-based perovskite oxides, that show a dramatic change of electrical resistance (conductance) in the presence of a magnetic field (28, 29). The application of an external magnetic field on such materials strongly enhances the electrical conductivity by orders of magnitude near the metal–insulator (MI) transition temperature  $T_{MI}$  (coupled to the Curie temperature  $T_C$ ), giving rise to the CMR effect (30, 31). The CMR property is a result of a competition between ferromagnetic interactions mediated by hopping of electron charge carriers—the double exchange mechanism (Fig. 8) (11, 12), and

antiferromagnetic superexchange interactions (Fig. 7) between localized spins of magnetic ions. In a certain range of doping in  $T_{1-x}D_x\text{MnO}_3$  (where  $T$  is a trivalent rare-earth ion, and  $D$  is a divalent alkali metal ion) with  $x = 0.2\text{--}0.4$ , the ground state is ferromagnetic, and the paramagnetic-to-ferromagnetic transition is accompanied by the CMR effect. The CMR can be viewed as the magnetic-field induced transformation from the long-range charge-/orbital-ordering or its short-range fluctuation, to the competing ferromagnetic metallic phase (32). The balance between these competing interactions as well as different structural and magnetic phases can be effectively tuned via the choice of trivalent rare-earth ions  $T$  (often  $T = \text{La, Pr, Nd, and Sm}$ ) and divalent alkali metal ions  $D$  (often  $D = \text{Sr, Ca, and Ba}$ ) elements in the  $A$ -sites of the mixed-valence perovskite manganites  $T_{1-x}D_x\text{MnO}_3$ , and their ratio that decides the relative fraction of  $\text{Mn}^{3+}$  and  $\text{Mn}^{4+}$ . The CMR technology is especially important in the disk read-and-write heads, and high-density data storage hard drive.

## II.6 Strain and interfacial effects in thin-film perovskites

Besides the intrinsic interplay of charge, spin, and orbital ordering superimposed by lattice effects in perovskites, the possibility of external modification of properties by epitaxial strain or artificial boundaries in thin-films of perovskites potentially generates novel electrical, optical, and magnetic properties. Recent advances in materials processing have led to the synthesis of low-dimensional perovskite oxides, namely, epitaxial ultra-thin films and free-standing nano/microwires. The thin-film perovskites are of a special requirement for device applications. Unlike bulk materials, the properties and functionalities of thin-film systems can be significantly tuned through an external strain. For example, strain effects play a major role in determining the magnetic and electronic properties of the thin films of rare-earth CMR manganites  $T_{1-x}D_x\text{MnO}_3$ . The investigation of the  $\text{La}_{0.88}\text{Sr}_{0.1}\text{MnO}_3$  films with several thicknesses reveals that a film of 240 nm thick behaves like its bulk material (antiferromagnetic insulator) whereas, the thin films (62 nm and 10 nm) show ferromagnetic metallic properties at low temperatures (Fig. 9)(33).

In another example, we describe here that the strain effect can lead to a significant enhancement of the ferroelectric transition temperature with the increasing misfit strain of the thin films of  $\text{BaTiO}_3$ . The  $\text{BaTiO}_3$  thin films grown on  $\text{GdScO}_3$  and  $\text{DyScO}_3$  substrates show a misfit strain of about  $\sim 1.0\%$  and  $\sim 1.7\%$ , respectively. The enhancement of ferroelectric transition temperature is reported from  $\sim 130^\circ\text{C}$  (for bulk) to  $\sim 400$  and  $\sim 540^\circ\text{C}$  for thin films with misfit strains of  $\sim 1.0\%$  and  $\sim 1.7\%$ , respectively.

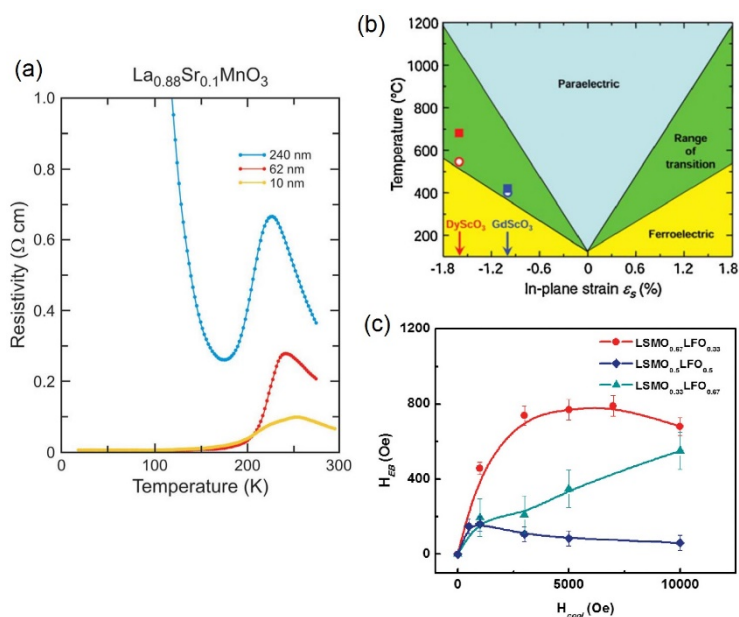


**Figure 9:** (a) Temperature-dependent resistivity curves for thin films of  $\text{La}_{0.88}\text{Sr}_{0.1}\text{MnO}_3$ . (b) The epitaxial strain–temperature phase diagram of  $\text{BaTiO}_3$  thin films. Wide transition temperature ranges (green region) appear due to the variation of reported coefficients. (c) Cooling field effect on the exchange bias behavior of  $(\text{LSMO})_{1-x}:(\text{LFO})_x$  films. (Reproduced with permission from (b) Choi *et al.*, *Science*, 306, 1005 (2004). Copyright 2004 by the American Association for the Advancement of Science. (a) Razvi *et al.*, *Appl. Phys. Lett.* 76, 155 (2000), (c) Fan *et al.*, *APL Materials* 4, 076105 (2016) Copyright 2000 and 2016 by the American Institute of Physics. )

It is also reported that the strained thin film has a remanent polarization; 250% higher than that of the bulk  $\text{BaTiO}_3$  single crystals (34). The epitaxial strain–temperature dependent phase diagram on the evolution of ferroic states in  $\text{BaTiO}_3$  is shown in Fig. 9(b). Besides, the heterostructures of transition metal perovskite oxides provide novel electronic and magnetic interface phenomena. For example, the metallic behavior in  $\text{SrTiO}_3/\text{LaAlO}_3$  perovskite superlattices is reported as compared to the Mott insulator and a band insulator of the individual components., respectively (35). This novel observation is caused by charge redistribution at polar/nonpolar interfaces. Another interfacial phenomenon of the heterostructure is the exchange bias, where a strong out-of-plane exchange bias ( $\sim 800$  Oe) appears in the FM/AFM

hetero-interfaces composed of aligned nanocomposite of perovskites  $(\text{La}_{0.7}\text{Sr}_{0.3}\text{MnO}_3)_{1-x} : (\text{LaFeO}_3)_x$  ( $x = 0.33, 0.5, \text{ and } 0.67$ ) based thin films (Fig. 9(c)). The disordered spin-glass states at the  $\text{La}_{0.7}\text{Sr}_{0.3}\text{MnO}_3 / \text{LaFeO}_3$  interfaces, related to magnetic frustration, are responsible for the exchange bias effect, where the interfacial frozen spins generate an additional torque on the  $\text{La}_{0.7}\text{Sr}_{0.3}\text{MnO}_3$  FM spins (36).

## II.7 Perovskites nanostructures

The functional properties of the perovskites can be well enhanced/tuned by making the particle size in the nanometer scale. Nanostructuring offers unique features viz. a large surface area, extensive porous structures, confinement effects, strong absorption, and photoluminescence, as well as controlled transport and charge-carrier mobility. These features together with the unique tunability in their composition, and shape make perovskite nanocrystals efficient for various applications; particularly as energy-materials (such as photovoltaics, thermoelectrics, batteries, supercapacitor and hydrogen storage systems), catalysts, (in oxygen reduction and hydrogen evolution reactions, lower activation energy, and high electron transfer kinetics), fuel cells, ion conductors, and electrochemical sensing (of alcohols, glucose, hydrogen peroxide, gases, and neurotransmitter). One of the specific examples of the tunable properties of nanostructure perovskite is that the combination of halide compositional modulations, as well as quantum size effects on the  $\text{CsPbX}_3$  ( $X = \text{Cl, Br, and I}$ ) nanoparticles, results into an optical emission over an entire visible spectral region of 410–700 nm (37) (Fig. 10).

## II.8 Applications of perovskites

Perovskite materials have been widely used in commercial device applications. The high stability of the perovskite structure as well as its flexibility to maintain a large oxygen vacancy concentration, makes perovskites suitable for electrodes, electrolyte as well as interconnecting material of a solid oxide fuel cell (SOFC) (38, 39). Perovskite materials are also widely used in piezoelectric sensor [ $\text{PbTiO}_3$ ,  $\text{Pb}(\text{Zr, Ti})\text{O}_3$  (PZT),  $\text{LiNbO}_3$ ,  $\text{LiTaO}_3$ ], light-emitting diodes (LEDs) (40), photovoltaic, photo-detectors (41), nano-lasers, waveguides, field-effect transistors (42), gas sensors [ $\text{LaCoO}_3$  and its derivatives as CO sensor,  $(\text{La/Sr})\text{FeO}_3$  and  $\text{LaMnO}_3$  as ethanol sensor, and  $\text{LaFeO}_3$  and  $\text{SmFeO}_3$  as  $\text{NO}_2$  sensor], glucose sensor, neurotransmitters sensor [nanostructure  $\text{LaFeO}_3$  and carbon paste electrode modified with  $\text{SrPdO}_3$  for dopamine sensor] and so on.

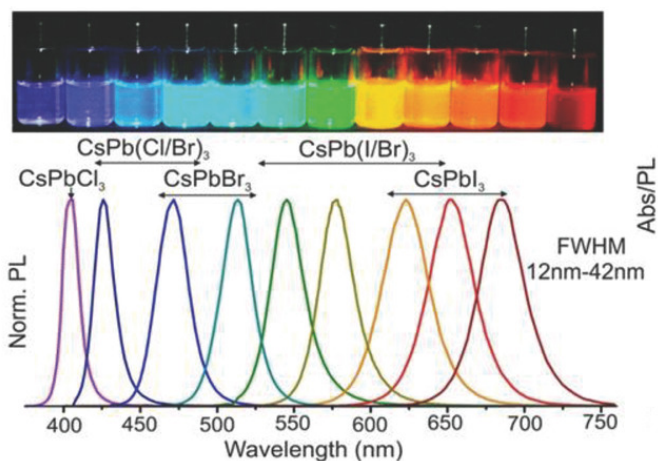


**Figure 10:** The color tuning of the perovskite nanocrystals of  $\text{CsPbX}_3$  ( $X = \text{Cl}, \text{Br}, \text{and I}$ ) with size- and composition. Colloidal solutions in toluene under UV lamp ( $\lambda = 365 \text{ nm}$ ) and the representative PL spectra are also shown. (Reproduced with permission from Kulkarni *et al.*, *Small Methods* 3, 1800231 (2019). Copyright 2018 WILEY-VCH Verlag GmbH & Co., Weinheim).

## II.9 Synthesis methods of perovskite compounds

The perovskites can be prepared in various forms (powder, crystal, and thin-film forms) by using a wide range of synthesis methods including the most conventional high-temperature solid-state reaction method, the microwave synthesis method (low temperature and low preparation time), and the wet chemical methods (solution preparation included the sol-gel preparation, co-precipitation of metal ions using the precipitating agents like cyanide, oxalate, carbonate, citrate, hydroxide ions, *etc.*, and thermal treatment) (43). The thin films of perovskites can be prepared by a gas-phase preparation method including laser ablation, molecular beam epitaxy, dc sputtering, magnetron sputtering, electron beam evaporation, and thermal evaporation techniques. The single crystals of several families of perovskite compounds can be synthesized from molten alkali carbonates or other fluxes, such as hydroxides or halides. Large single crystals (several centimeters long) of manganites and other oxides have also been grown by an optical floating zone technique.

### III. Magnetic Properties and Magneto-structural Correlations

The magnetic moment in an ion is formed by electron–electron interaction and correlation. Whereas, the magnetic ordering in a material is controlled by the exchange interactions which are a result of an orbital hybridization or a bonding between such ions having magnetic moments. For example, an antiferromagnetic (AFM) superexchange interaction is a result of the energy lowering of the occupied states due to its hybridization with the excited states (11, 44). For the transition-metal ions, the orbital hybridization depends on both the geometrical arrangement of atoms and the mode of the orbital occupation or orbital ordering. For example, in the Jahn–Teller effect [4], there is a strong coupling between orbital ordering and the lattice distortion. In this way, magnetism, orbital ordering, and lattice distortion are intrinsically correlated (45, 46). The perovskites based on the transition metal oxides serve as a playground for demonstrating several novel magnetic phenomena. Some of these are discussed below.

#### III.1 Role of site disorder on magnetism in the mixed-metal perovskite $\text{LaMn}_{0.5}\text{Co}_{0.5}\text{O}_3$

The mixed metal oxide perovskite  $\text{LaMn}_{0.5}\text{Co}_{0.5}\text{O}_3$  shows interesting magnetic properties where the magnetic ordering temperature  $T_C$  varies from 125 K to 230 K depending on the sample preparation procedure. For example, the  $\text{LaMn}_{0.5}\text{Co}_{0.5}\text{O}_3$  samples prepared at 700 °C and 1300 °C show the magnetic ordering at  $T_C = 225$  K and 150 K, respectively (Fig. 11) (47). An early study based on the x-ray diffraction reported that the low- $T_C$  sample (LTc) crystallized in the monoclinic structure with a space group  $P2_1/n$  (Fig. 12), while the high- $T_C$  sample (HTc) crystallized in the rhombohedral structure with space group  $R-3C$  (48). We add here that a detailed neutron diffraction study (47) reveals that both the samples crystallize in the monoclinic structure (space group  $P2_1/n$ ), however, there is a significant difference in the  $B$  site ordering which leads to the observed variation in the magnetic ordering temperature  $T_C$ .

In the monoclinic crystal structure with a space group  $P2_1/n$ , the  $B$  cations (Mn and Co) are situated at two crystallographically distinguished Wyckoff positions ( $2c$  and  $2d$  sites, respectively) (Fig. 12). The magnetic property strongly depends on the relative occupations of the Mn and Co ions at the  $2c$  and  $2d$  sites. The relative occupations

decide the local magnetic exchange interactions in the compound, either Mn-Mn or Mn-Co or Co-Co.

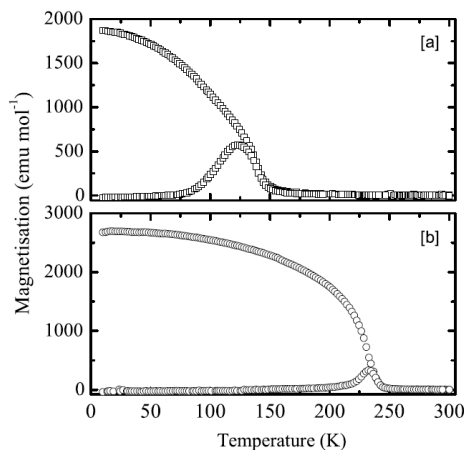


**Figure 11:** Temperature-dependent dc magnetization curves for the (a) LTc and (b) HTc  $\text{LaMn}_{0.5}\text{Co}_{0.5}\text{O}_3$  compound measured under 100 Oe. (Reprinted with permission from Viswanathan *et al.*, *J. Phys.: Condens. Matter* 22 346006 (2010). Copyright 2010 Institute of Physics.)

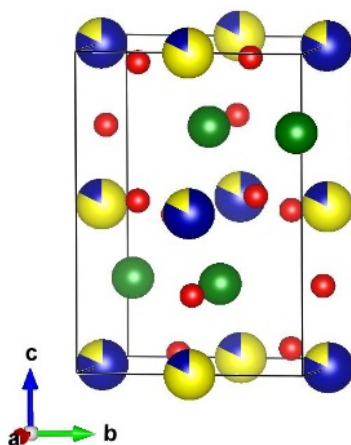


**Figure 12:** The representative crystal structure of monoclinic  $\text{LaMn}_{0.5}\text{Co}_{0.5}\text{O}_3$  with the space group  $P2_1/n$ . The relative occupations of the Co and Mn ions at the two crystallographically distinguished Wyckoff positions (2c and 2d sites, respectively) are shown by the blue and yellow portions, respectively.

As the atomic number  $Z$  values of Mn ( $Z=25$ ) and Co ( $Z=27$ ) are close, the cation distributions to the  $2c$  and  $2d$  sites are insensitive to the x-ray diffraction. Whereas, as the neutron scattering lengths  $b$  ( $= -0.3730 \times 10^{-15}$  m and  $0.2490 \times 10^{-15}$  m for Mn and Co, respectively) are quite different, the neutron

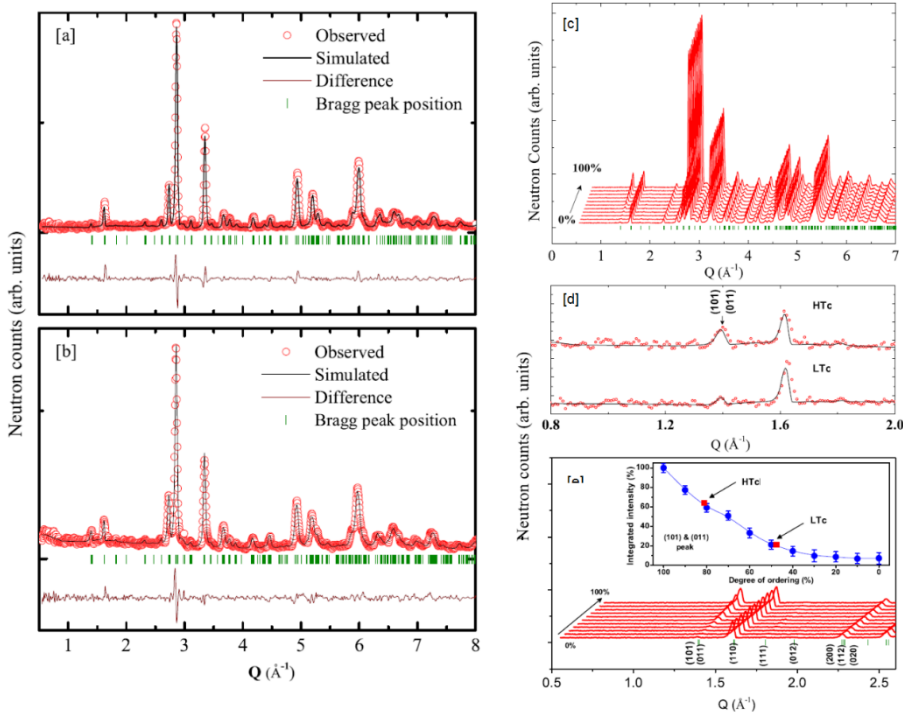


**Figure 13:** Neutron diffraction patterns for the (a) LTC and (b) HTC  $\text{LaMn}_{0.5}\text{Co}_{0.5}\text{O}_3$  compounds at 300 K. (c) Calculated neutron diffraction patterns for various values of cation ordering. (d) Expanded region of experimental diffraction patterns over the (101) and (011) peaks. (e) Low  $Q$  region of the calculated diffraction patterns. The inset shows the integrated intensity of (101) and (011) Bragg peaks as a function of cation ordering with the positions of the LTC and HTC compounds. (Reprinted with permission from Viswanathan *et al.*, *J. Phys.: Condens. Matter* 22 346006 (2010). Copyright 2010 Institute of Physics.)

diffraction technique is very sensitive to the cation distributions. The experimental neutron diffraction patterns clearly show a difference in the intensity of the (101) and (011) Bragg peaks at  $Q = 1.4$  and  $1.6 \text{ \AA}^{-1}$  [Fig. 13(a) and 13(b)] for the LTC and HTC samples. The degree of cation ordering can be estimated from the intensity of the

(101) and (011) Bragg peaks. The degree of cation ordering is defined by the relative percentage of Mn and Co ions at the  $2c$  and  $2d$  crystallographic sites, respectively; i.e., 0% for completely random distributions of the Mn and Co at both the sites, and 100% when Mn and Co are located at the individual sites. The calculated neutron diffraction patterns for 0–100% cation ordering are shown in Fig. 13(e). The relative integrated intensity of the (101) Bragg peak to the (011) Bragg peaks is found to be higher for a better percentage of cation ordering, like in the HTc as compared to that in the LTc [Fig. 13(d-e)] The degrees of order, estimated from the experimental data, are found to be 81.2% for the HTc and 47.6% for the HTc and LTc samples, respectively [Fig. 13(e)]. Such cation ordering is responsible for the different magnetic ordering temperatures in the perovskites under study (49). It is also reported that the degree of cation ordering in perovskite systems depends strongly on the synthesis parameters, such as annealing/heating time (50) and temperature (51).

### III.2 Tunable magnetism and magneto-structural correlations in $\text{La}_{1-x}\text{Ce}_x\text{CrO}_3$

The rare earth chromium-based perovskites show interesting magnetic properties and play an important role to understand many exotic magnetic properties (22, 23, 52-56). Here we present the results of the Ce doped  $\text{LaCrO}_3$ , having an orthorhombic crystal structure with space group  $Pbnm$  as shown in Fig. 14. With the Ce substitution at the La site, the compounds show an unusual magnetic behavior which strongly depends on the relative concentration of the  $\text{La}^{3+}$  and  $\text{Ce}^{3+}$  ions at the A site (22, 23, 55, 56).

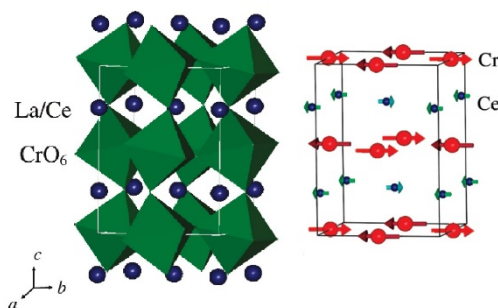


**Figure 14:** The crystal and magnetic structures of the perovskite compounds  $\text{La}_{1-x}\text{Ce}_x\text{CrO}_3$ . (Reprinted with permission from Shukla *et al.*, *Inorg. Chem.*, 48, 11691 (2009). Copyright 2009 American Chemical Society.)

The ionic sizes of the  $\text{La}^{3+}$  and  $\text{Ce}^{3+}$  ions are very close (the ionic radii of  $\text{La}^{3+}$  and  $\text{Ce}^{3+}$  are 1.03 Å and 1.01 Å, respectively). However, their electronic configurations are different, where, the  $\text{La}^{3+}$  ( $4f^0$ ) does not contain any  $f$  electron and carries spin  $S=0$ . On the other side,  $\text{Ce}^{3+}$  ( $4f^1$ ) has one unpaired electron in the  $4f$  shell and carries  $S=1/2$ . Therefore, the change of magnetic behavior is expected due to a varying magnetic coupling between  $A$  (Ce/La) and  $B$  (Cr) sites with changing the Ce concentration. The zero-field-cooled (ZFC) magnetization curves for all of the compounds ( $0.1 \leq x \leq 1.0$ ) (Fig. 15) show a peak (for example, at 281.5 K for the composition  $x = 0.1$ ) corresponding to an AFM ordering of the  $\text{Cr}^{3+}$  spins (55). The Néel temperature of the AFM ordering shifts linearly down from 281.5 to 257 K with the increase of the  $\text{Ce}^{3+}$  concentration from 0.1 to 1.0 (Fig. 15). Unlike the ZFC curves, the temperature-dependent field-cooled (FC) curves show remarkable variations with the changing  $\text{Ce}^{3+}$  concentration.

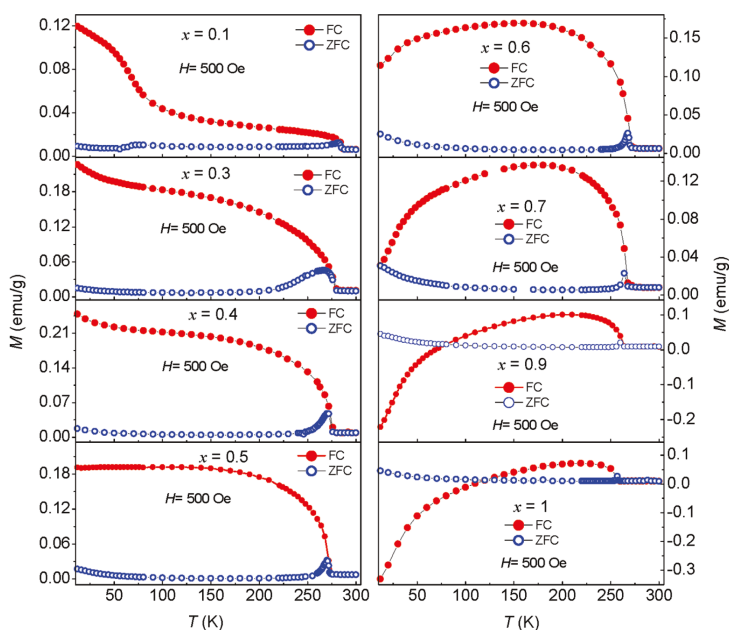


**Figure 15:** Temperature-dependent zero-field-cooled (ZFC) and field-cooled (FC) magnetization curves for the  $\text{La}_{1-x}\text{Ce}_x\text{CrO}_3$  compounds measured under 500 Oe. (Reprinted with permission from Shukla *et al.*, *Inorg. Chem.*, 48, 11691 (2009). Copyright 2009 American Chemical Society.)

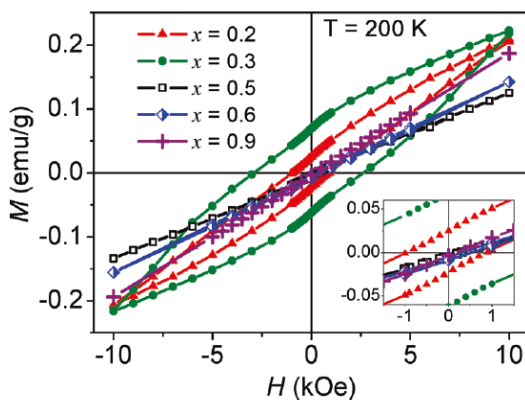


**Figure 16:** Isothermal magnetization ( $M$  vs  $H$ ) curves at 200 K for the  $\text{La}_{1-x}\text{Ce}_x\text{CrO}_3$  compounds. (Reprinted with permission from Shukla *et al.*, *Inorg. Chem.*, 48, 11691 (2009). Copyright 2009 American Chemical Society.)

For the samples with higher  $\text{Ce}^{3+}$  concentrations ( $x \geq 0.5$ ), the FC magnetization curves show a broad maximum (with decreasing temperature, FC magnetization first increases sharply at the  $T_N$  and then reaches a maximum and thereafter decreases). Whereas, for the  $x \leq 0.4$  samples, the FC magnetization somewhat increases monotonically with decreasing temperature below the  $T_N$  without any sign of a downturn. The most interesting behavior appears for  $x \geq 0.8$  where the FC magnetization becomes negative below  $\sim 70$  K (55). A similar kind of behavior is also reported for other perovskite compounds  $\text{La}_{1-x}\text{Pr}_x\text{CrO}_3$  (57),  $\text{La}_{1-x}\text{Gd}_x\text{MnO}_3$  (58),  $\text{NdMnO}_3$  (59), etc. Such negative magnetization can be attributed to the different magnetic ordering temperatures of the A ( $\text{Ce}^{3+}$ ) and B ( $\text{Cr}^{3+}$ ) sites for the compounds  $\text{La}_{1-x}\text{Ce}_x\text{CrO}_3$  and their temperature dependence under an externally applied magnetic field in the presence of sublattice magnetocrystalline anisotropies (discussed in detail in the next section). The isothermal magnetization curves for the  $\text{La}_{1-x}\text{Ce}_x\text{CrO}_3$  compounds in the AFM ordered state yield interesting behaviors where only  $x=0.2$  and  $0.3$  compounds show a clear hysteresis (maximum for the  $x=0.3$  compound) (Fig. 16). The  $M$  vs  $H$  curves for all the compounds across the series do not show any sign of saturation up to 1 T. The observed hysteresis appears due to a canting of the  $\text{Cr}^{3+}$  spins which increases initially with the Ce substitution (up to  $x=0.3$ ) and then decreases with further Ce substitution and becomes zero for  $x \geq 0.9$ .

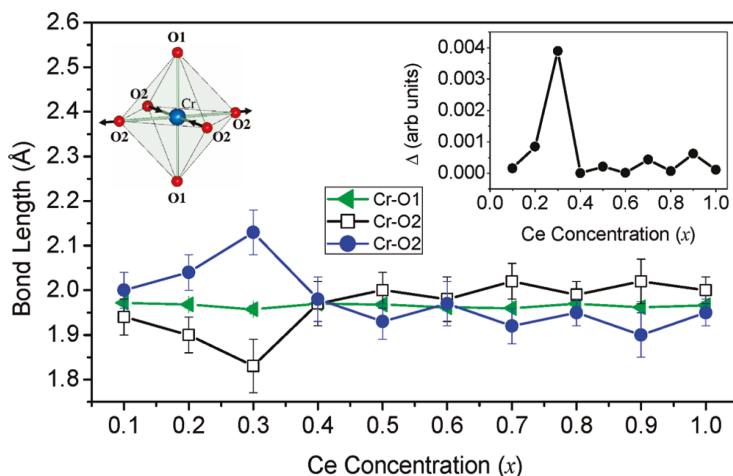


**Figure 17: Cr-O bond lengths of the  $\text{La}_{1-x}\text{Ce}_x\text{CrO}_3$  compounds as a function of Ce concentration. (Left inset) A schematic for expansion and contraction of Cr-O2 bond lengths in the basal plane of  $\text{CrO}_6$  octahedra. (Right inset) Octahedral distortion parameter as a function of Ce concentration in  $\text{La}_{1-x}\text{Ce}_x\text{CrO}_3$ . (Reprinted with permission from Shukla *et al.*, *Inorg. Chem.*, 48, 11691 (2009). Copyright 2009 American Chemical Society.)**

The detailed crystal structural study by x-ray diffraction divulges the origin of such spin canting [appears over the limited substitution range ( $x = 0.1-0.4$ )] as the local octahedral distortion at the *B* (Cr) site of the perovskite structure. Both the bond lengths in the basal plane (two Cr-O2 bond lengths) show an anomaly over the Ce concentration range  $0.1 < x < 0.4$  with a maximum for the compound  $x = 0.3$  where the difference in their values is also maximum (Fig. 17). Such differences in the values of the bond lengths reveal a distortion in the  $\text{CrO}_6$  octahedra. The quantification of the distortion is made by the following equation

$$\Delta = (1/6) \sum_{i=1}^6 \left( \frac{d_i - \langle d \rangle}{\langle d \rangle} \right)^2 \quad (3)$$

where  $\langle d \rangle$  is the average bond length and  $d_i$  is the  $i^{\text{th}}$  bond length. The  $\Delta$  vs. Ce concentration curve shows a peak at  $x=0.3$  and remains nearly zero above the  $x = 0.4$ . The ferromagnetic behavior in  $\text{La}_{1-x}\text{Ce}_x\text{CrO}_3$  follows a similar trend like distortion, where with the increasing Ce concentration the maximum hysteresis is found for the  $x=0.3$  compound and no hysteresis is found above the  $x = 0.4$  compound. Therefore the origin of the ferromagnetism in  $\text{La}_{1-x}\text{Ce}_x\text{CrO}_3$  is regarded as the octahedral distortion.

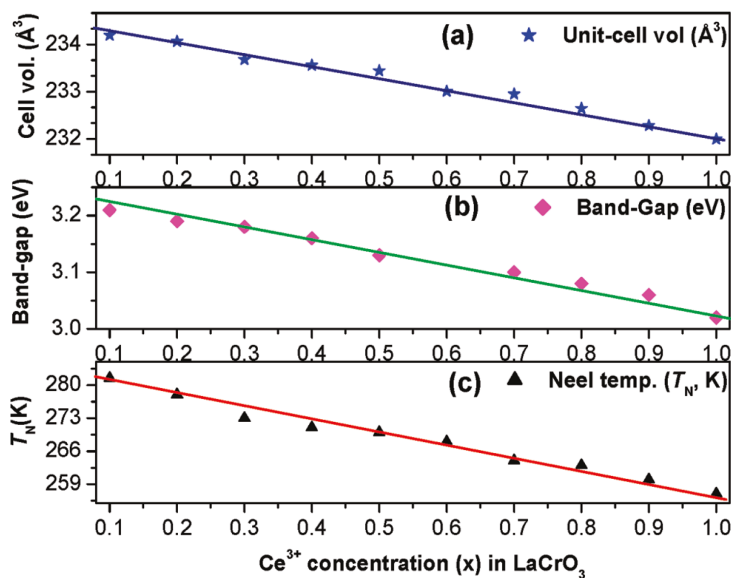


**Figure 18:** (a) unit-cell volume, (b) band-gap, and (c) Neel temperature,  $T_N$ , as a function of  $\text{Ce}^{3+}$  concentration ( $x$ ) in  $\text{La}_{1-x}\text{Ce}_x\text{CrO}_3$ . (Reprinted with permission from Shukla *et al.*, *Inorg. Chem.*, 48, 11691 (2009). Copyright 2009 American Chemical Society.)

Moreover, the optical properties, as like the magnetic properties, have also been found to be strongly coupled to the crystal structure of  $\text{La}_{1-x}\text{Ce}_x\text{CrO}_3$ . Figure 18 shows the Ce concentration dependence of the unit cell volume, bandgap, and Néel temperature. Remarkably, all of these parameters show an identical decreasing trend with the increasing  $\text{Ce}^{3+}$  concentration where the unit cell volume decreases from 233.97(4) to 231.95(4) Å<sup>3</sup>, the bandgap decreases from 3.21 to 3.02 eV, and the  $T_N$  decreases from 281.5 to 257 K for the variation of  $x$  from 0.1 to 1.0, respectively.

### III.3 Role of magnetocrystalline anisotropy on negative magnetization and magnetization compensation in $\text{NdMnO}_3$

One of the interesting magnetic phenomena in perovskites is the negative magnetization where the net magnetization in a material appears opposite to the applied magnetic field in certain conditions. The state of the negative magnetization (with a positive differential susceptibility,  $\partial M/\partial H$ ) is different from a diamagnetic state

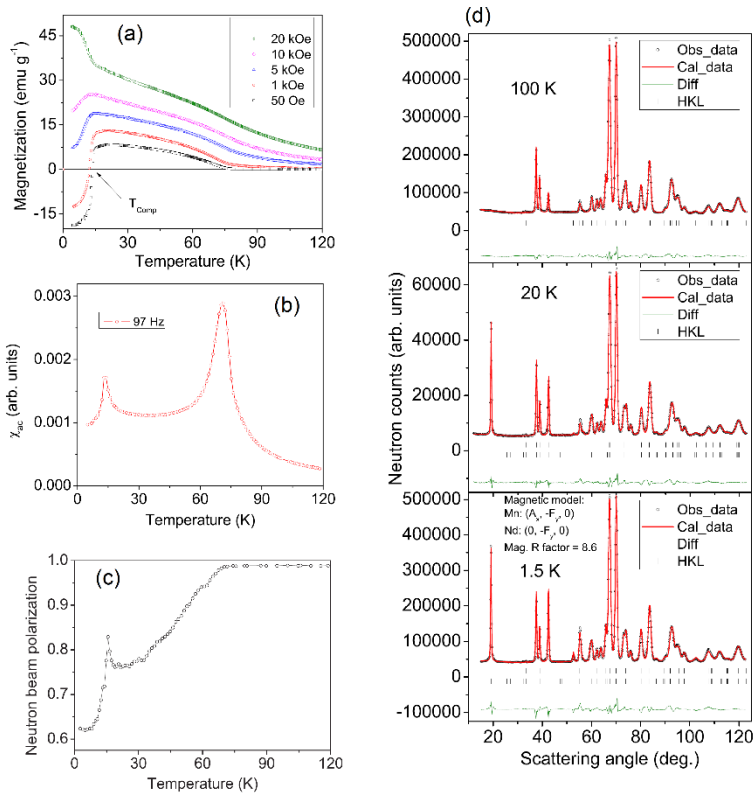


**Figure 19:** (a) Temperature-dependent field-cooled dc magnetization curves for NdMnO<sub>3</sub> at various cooling fields. (b) Temperature-dependent real part of the ac susceptibility ( $\chi_{ac}$ ) curve for NdMnO<sub>3</sub> measured at 97 Hz. (c) Temperature-dependent transmitted neutron beam polarization curve for the NdMnO<sub>3</sub> compound. (d) Rietveld refined neutron diffraction patterns measured at 100, 20, and 1.5 K covering three magnetic regimes of NdMnO<sub>3</sub> compound. The positions of the magnetic Bragg peaks (middle and bottom panels) are shown by the second row of vertical bars. (Reprinted with permission from Kumar *et al.*, Phys. Rev. B., 96, 014427 (2017). Copyright 2017 American Physical Society.)

(with a negative differential susceptibility) that occurs in the case of superconducting as well as diamagnetic materials. The phenomenon of magnetization reversal has a

special importance due to its practical utilization in magnetic memory, and magnetocaloric and spin resolving devices (60). Such phenomena have been found in several magnetic materials in which perovskites take a lead role (60). We discuss below the microscopic origin of this novel phenomenon based on a model compound  $\text{NdMnO}_3$  perovskite (59). The  $\text{NdMnO}_3$  compound possesses an orthorhombic (space group:  $Pnma$  or equivalent space group  $Pbnm$ ) crystal structure at room temperature. Within the orthorhombic crystal structure, the Nd and Mn cations are located at the  $4c$  ( $x, 1/4, z$ ) and  $4b$  ( $0, 0, 1/2$ ) crystallographic positions, respectively, whereas the oxygen anions are located at the  $4c$  ( $x, 1/4, z$ ) and  $8d$  ( $x, y, z$ ) crystallographic sites. The bulk properties studies (dc magnetization, ac susceptibility, and specific heat) reveal magnetic phase transitions at around 75 K ( $T_C$ ) and 15 K (Fig. 19). Magnetization reversal or negative magnetization is found in the  $M$  vs  $T$  curves (Fig. 19). With decreasing temperature, the temperature-dependent magnetization for  $H < 1$  kOe starts decreasing below 20 K, and becomes negative (opposite to the direction of the measurement field) below the compensation temperature ( $T_{\text{Comp}}$ ) of  $\sim 15$  K where the magnetization value becomes zero. The neutron diffraction study reveals the microscopic origin of the observed magnetization reversal in the temperature-dependent dc magnetization study across 15 K (59) [Fig. 20].

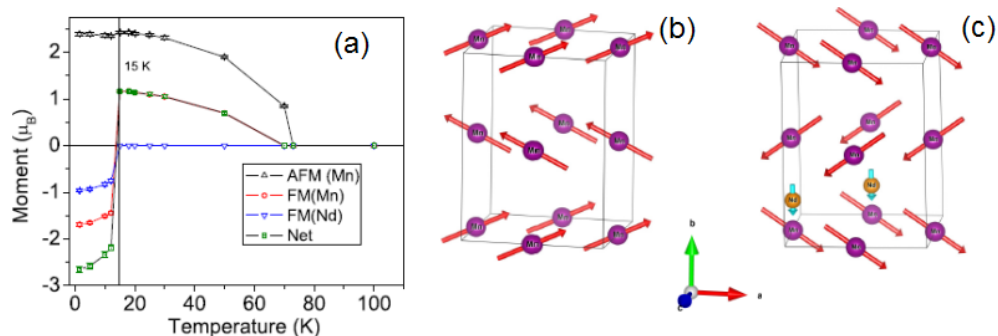


**Figure 20:** (a) The sublattice and net ordered magnetic moments for  $\text{NdMnO}_3$ . (b) and (c) Magnetic structures for  $\text{NdMnO}_3$  at 20 and 1.5 K, respectively. (Reprinted with permission from Kumar *et al.*, *Phys. Rev. B.*, **96**, 014427 (2017). Copyright 2017 American Physical Society.)

Neutron diffraction experiments reveal that the transition at 75 K corresponds to the ordering of the Mn sublattice with  $(Ax, Fy, 0; Pnma$  setting) type spin arrangement with a net FM moment along the  $b$  axis. The second magnetic transition

at 15 K corresponds to the ordering of the Nd sublattice with a  $(0, -F_y, 0)$  type of spin arrangement, and it is accompanied by the reorientation of the Mn spins (by  $180^\circ$ ) from  $(A_x, F_y, 0)$  to  $(A_x, -F_y, 0)$ . The temperature dependence of the derived magnetic moments is depicted in Fig. 20. The magnetic structures obtained from the neutron diffraction study at temperatures above (20 K) and below (1.5 K) the Nd ordering temperature (15 K) are shown in Figs. 20(b) and 20(c), respectively. With the decreasing temperature below 73 K, the net FM moment of Mn ions aligns itself along the applied field direction, and a positive magnetization results down to 15 K in the field cooled dc magnetization measurement [Fig. 20(a)]. Below 15 K, the magnetic ordering of the Nd moments occurs along the  $-ve$   $b$  axis along with a reorientation of the Mn spins that results in a net FM moment opposite to the applied field direction. The magnetocrystalline anisotropy is the driving force for the magnetic ordering of the Nd moments to adopt the  $(0, -F_y, 0)$  arrangement that causes a change of the net FM moment of  $\text{NdMnO}_3$  from a positive value (above 15 K) to a negative value (below 15 K). Moreover, crystal structural distortions are found at 15 K with the spin reorientation transition (Fig. 21). The clear anomalies are found for the lattice constants  $b$  and  $c$ , as well as for the Mn-O1-Mn and Mn-O2-Mn bond angles (mainly responsible for magnetic exchange interaction paths) around 15 K. Below 15 K, a strong distortion in the  $\text{MnO}_6$  octahedra is reported. The above observations strongly indicate a large magneto-structural coupling.

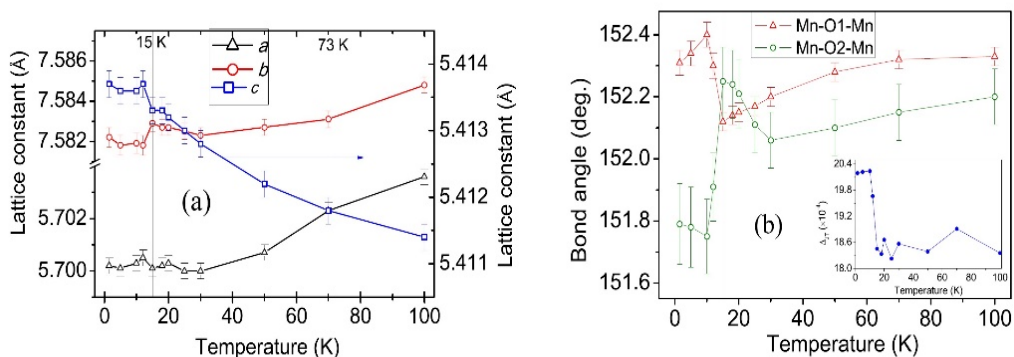


**Figure 21: The temperature variation of (a) lattice parameters and (b) bond angles for  $\text{NdMnO}_3$  compound. The inset in (b) depicts the variation of the Jahn-Teller distortion ( $\Delta_{JT}$ ) as a function of temperature. (Reprinted with permission from Kumar *et al.*, Phys. Rev. B., 96, 014427 (2017). Copyright 2017 American Physical Society.)**

## IV. Multiferroic Perovskites and Structural Correlations

In this section we discuss the important role of perovskites on realizing and understanding the fascinating phenomenon of multiferroics, emphasizing the relations between the crystal structure and the possible combination of ferromagnetism and ferroelectricity via the strong magnetoelectric coupling. The origin of ferroelectricity in perovskite is structural instability which results in breaking of centrosymmetry and/or deformation of perovskite, commonly known as the second-order Jahn-Teller Effect (61). For instance, in the classical ferroelectric material  $\text{BaTiO}_3$ , while cooling,  $\text{Ti}^{4+}$  shifts from the ideal position and the crystal structure stabilizes in the tetragonal, orthorhombic or rhombohedral phases with different spontaneous electrical polarization at the different temperature regimes (62). On the other hand, in perovskites, the magnetism is governed by the quantum-mechanical exchange interactions, viz., double exchange and superexchange interactions. In general, the perovskite compounds with double exchange interactions, resulting in ferromagnetic ordering (12, 13), can hardly be multiferroic materials due to the hopping electrons which screen the long-range Coulomb interactions. In contrast, the superexchange interaction in perovskite-type oxides can induce either ferromagnetism or antiferromagnetism (63, 64). Moreover, perovskite compounds are commonly insulators, giving ways to combine the ferroelectricity and magnetism.

### IV.1 Magnetic ordering and spin-phonon coupling in multiferroic $\text{Y}_{1-x}\text{Tb}_x\text{MnO}_3$

The rare-earth manganite  $\text{RMnO}_3$  perovskites reveal both type-I and type-II multiferroics. The  $\text{RMnO}_3$  perovskites having a large  $R$  ionic radius ( $R = \text{La-Dy}$ ) crystallize in the orthorhombic structure ( $o\text{-RMnO}_3$ ) with  $Pbnm$  space group and are of the type-II multiferroics (65). On the other hand,  $\text{RMnO}_3$  perovskites with a small  $R$  ionic radius ( $R = \text{Ho-Lu, Y, or Sc}$ ) yield a hexagonal structure ( $h\text{-RMnO}_3$ ) with  $P6_3cm$  symmetry (66) and are of the type-I multiferroics. For the  $o\text{-RMnO}_3$  type, the ferroelectric polarization in  $\text{RMnO}_3$  relates to the non-collinear incommensurate modulated magnetic order accompanied by a magnetoelastically induced lattice modulation, which breaks the spatial inversion symmetry and induces the magnetoelectricity (16). For the  $h\text{-RMnO}_3$  type, the ferroelectric phase is characterized by a buckling of the layered  $\text{MnO}_5$  polyhedra, accompanied by the displacement of the  $R$  ions, which leads to a net electric

polarization (67). The crystal structure of *h*-*RMnO*<sub>3</sub>; in particular *YMnO*<sub>3</sub> consists of non-connected layers of *MnO*<sub>5</sub> trigonal bipyramids corner-linked by the in-plane oxygen ions (*O*<sub>P</sub>), with apical oxygen ions (*O*<sub>T</sub>) forming the close-packed planes separated by a layer of *Y*<sup>3+</sup> ions (Fig. 22).

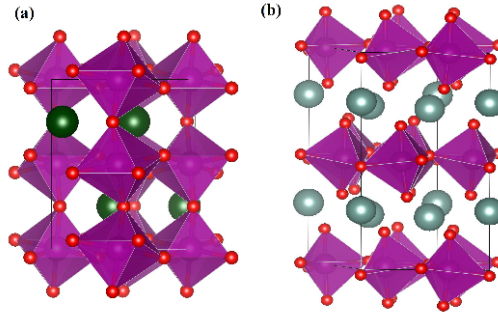


**Figure 22:** (a) Orthorhombic (*o*-*RMnO*<sub>3</sub>) and (b) hexagonal (*h*-*RMnO*<sub>3</sub>) crystal structure of multiferroic perovskite *RMnO*<sub>3</sub>.

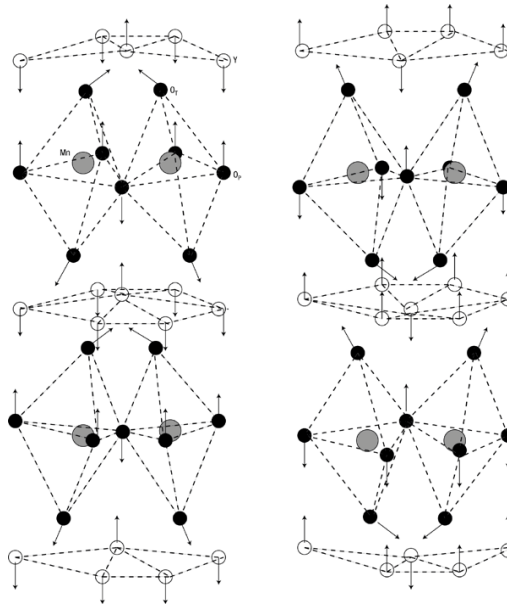


**Figure 23:** A schematic view of the crystal structure of *YMnO*<sub>3</sub> in the two enantiomorphous polarized states. Arrows indicate the directions of the atomic displacements from the centrosymmetric to the ferroelectric structure. (Reprinted with permission from Van Aken *et al.*, *Nature Mater.*, **3**, 164 (2004). Copyright 2004 Nature Publishing Group.)

It may be noted that the crystal structure of  $h$ - $\text{RMnO}_3$  is remarkably different from the cubic perovskite structure, which features corner-linked  $\text{MnO}_6$  octahedra to form a three-dimensional (3D) network. The paraelectric ( $P6_3/mmc$ ) to ferroelectric ( $P6_3cm$ ) transition is associated with the breaking of the mirror plane symmetry perpendicular to the hexagonal  $c$  axis with two major atomic displacements in the crystal structure. First: the buckling of the  $\text{MnO}_5$  bipyramids, and the second is the vertical shift of the Y ions away from the high-temperature mirror plane, while keeping the distance to  $\text{O}_T$  constant (Fig. 23). The magnetic long-range ordering in these compounds occurs at low temperatures ( $\sim$ below 100 K)

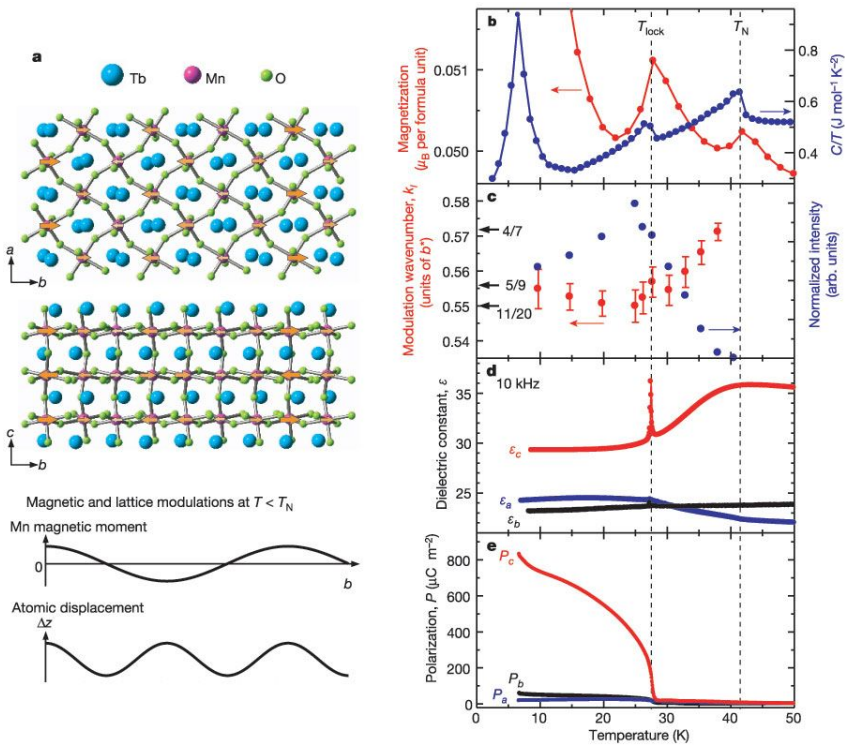


**Figure 24:** (a) A schematic crystal structure of  $\text{TbMnO}_3$  at room temperature (top). The Mn magnetic moments below  $T_N$  are shown by the orange arrows. (bottom) Spatial variation of Mn magnetic moment and atomic displacement ( $\Delta z$  //  $c$ ) along the  $b$  axis for  $T < T_N$ . Temperature-dependent (b) magnetization and specific heat, (c) wavenumber of lattice modulation  $k_i$ , (d) dielectric constant  $\epsilon$  at 10 kHz, and (e) electric polarization  $P$  along the principal axes. (Reprinted with permission from Kimura *et al.*, *Nature*, 426, 55 (2003). Copyright 2003 Nature Publishing Group.)

(68), and Mn spins form a non-collinear, so-called the  $120^\circ$  antiferromagnetic structure. The crystal structure of  $o$ -RMnO<sub>3</sub>, is an orthorhombically distorted perovskite structure (space group  $Pbnm$ ). The spin structure in TbMnO<sub>3</sub>, having the  $o$ -RMnO<sub>3</sub> structure, is a sinusoidal AFM ordering of the Mn<sup>3+</sup> moments below the  $T_N = 41$  K with a wave vector  $q = (0, k_s, 1)$  with respect to the  $Pbnm$  orthorhombic unit cell. The wavenumber  $k_s$  is incommensurate ( $\sim 0.295$ ) at  $T_N$  and decreases with decreasing temperature, becomes nearly constant (0.28) below 30 K ( $T_{lock}$ ). All temperature-dependent physical properties, such as magnetization ( $M$ ) under 0.5 T, specific heat divided by

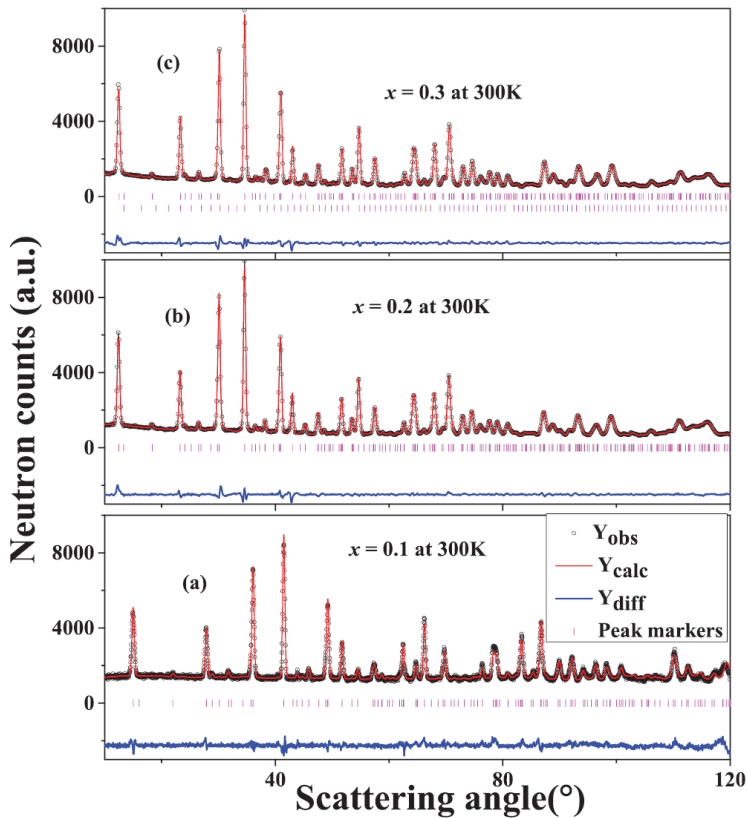


**Figure 25:** Rietveld refined neutron diffraction patterns at RT for the compounds  $Y_{1-x}Tb_xMnO_3$  with (a)  $x = 0.1$  (b)  $x = 0.2$  and (c)  $x = 0.3$ , respectively. The observed data, calculated patterns, and the difference patterns are shown by open black circles, red continuous curves, and blue continuous curves, respectively. Bragg peak positions are shown by magenta bars. (Reprinted with permission from Chakraborty *et al.* *J. Phys.: Condens. Matter* 29 155804 (2017). Copyright 2017 IOP Publishing Ltd.)

temperature ( $C/T$ ), the wavenumber of lattice modulation  $k_l$ , the normalized intensity of a super-lattice reflection at  $(0, k_l, 3)$ , and dielectric constant ( $\epsilon$ ) show an anomaly at this temperature where the magnetic modulation wave vector  $k_s$  is locked at a constant value (Fig. 24). The compound  $\text{TbMnO}_3$  becomes ferroelectric below  $T_{\text{lock}}$  where a finite spontaneous polarization appears along the  $c$  axis. The DM interaction is responsible for the modulated magnetic structure and the ferroelectricity in this compound (69). Thus the modulated magnetic structure, accompanied by a magnetoelastically induced lattice modulation, results in the emergence of ferroelectricity in the orthorhombic  $\text{TbMnO}_3$ .

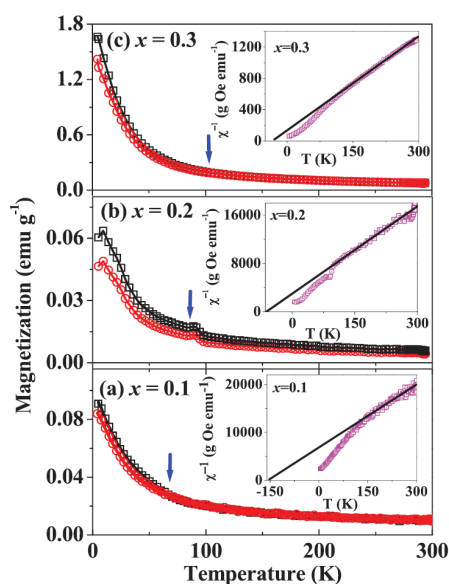


**Figure 26:** The temperature-dependent ZFC and FC magnetization curves, measured under an applied field of 200 Oe for the compounds  $\text{Y}_{1-x}\text{Tb}_x\text{MnO}_3$  with (a)  $x = 0.1$ , (b)  $x = 0.2$  and (c)  $x = 0.3$ . The blue arrow indicates the onset of magnetic ordering. Insets show  $\chi^{-1}$  versus  $T$  curves along with the linear fit (solid straight lines). (Reprinted with permission from Chakraborty *et al.* *J. Phys.: Condens. Matter* 29 155804 (2017). Copyright 2017 IOP Publishing Ltd.)

Now we discuss the intermediate situation between two different types of multiferroic compounds  $h\text{-YMnO}_3$  and  $o\text{-TbMnO}_3$ . The substitution of Tb at the Y-site of  $\text{YMnO}_3$  provides such an opportunity (70, 71). With the Tb substitution in  $\text{Y}_{1-x}\text{Tb}_x\text{MnO}_3$  up to a concentration of  $x=0.3$ , the crystal structural symmetry remains unchanged (hexagonal with space group  $P6_3cm$ ) (70). The room temperature neutron diffraction patterns for

the substituted compounds are shown in Fig. 25. Out of the two crystallographic sites (2a and 4b) of  $Y^{3+}$ , the  $Tb^{3+}$  ions are found to be exclusively residing at the 4b site with  $Y^{3+}$  ions for all three compositions,  $x = 0.1, 0.2,$  and  $0.3$ . The 2a site contains solely the remaining  $Y^{3+}$  ions. A monotonous decrease of the unit cell volume is found with the Tb substitution. Temperature-dependent Raman scattering measurements reveal a spin-phonon coupling for all three compositions. The temperature-dependent magnetization measurements (Fig. 26) suggest an increase of the magnetic ordering temperature with a relief of the magnetic frustration with the increasing  $Tb^{3+}$  concentration due to an elongation of the Mn-O-Mn bond angle.

## IV.2 Magneto-structural coupling in the hexagonal multiferroic $LuFeO_3$

We have discussed in an earlier section that the perovskite manganites play important roles to stabilize type-I and type-II multiferroics. Among them, hexagonal manganites (type-I) are fascinating due to high electric polarization and high ferroelectric transition temperature, however, their antiferromagnetic ordering temperatures are low ( $\sim$ below 100 K) and Mn spins couple feebly with its ferroelectric order to have a weak magnetoelectric coupling. Substitution of Mn with Fe has been proposed as one of the ways to increase the magnetic transition temperature as well as to enhance the coupling between the two order parameters. The higher values of both magnetization and ordering temperature are essential for practical device applications. In view of this, the isostructural hexagonal ferrites ( $h-RFeO_3$ ,  $R = Eu-Lu, Y,$  or  $Sc$ ) (72, 73) become a center of attention, as the magnetic ordering temperature is expected to be higher due to (i) the strong exchange coupling between  $Fe^{3+}$  ions compared with  $Mn^{3+}$  ions (74), and (ii) the high localized magnetic moment of Fe (75). However, the preparation of single-phase  $h-LuFeO_3$  is very challenging in the bulk form which is overcome through an optimized sol-gel synthesis condition (76).

Neutron diffraction study reveals the hexagonal crystal structure with  $P6_3cm$  space group which persists down to 6 K (Fig. 27). The  $h-LuFeO_3$  is ferroelectric at room temperature, with a paraelectric-to-ferroelectric transition temperature  $T_C \sim 1020$  K. The  $P-E$  loop measurements at room temperature confirm that  $h-LuFeO_3$  is an intrinsic ferroelectric material with remanent polarization  $P_r \sim 0.18 \mu C/cm^2$ . Further, a switchability of the polar behavior is reported using the piezoelectric force microscopy at room temperature, providing a strong evidence of ferroelectricity (77).

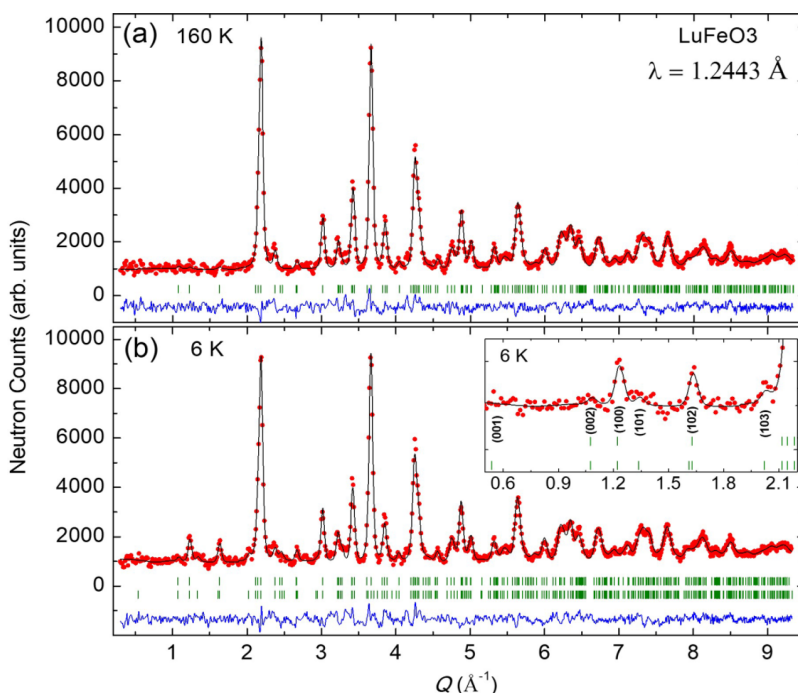


**Figure 27:** Rietveld refined neutron-diffraction patterns for h-LuFeO<sub>3</sub> at (a) 160 K (paramagnetic state) and (b) 6 K (magnetically ordered state), respectively. The inset of (b) shows the zoomed pattern at 6 K over the low-Q region. (Reprinted with permission from Suresh *et al.* Phys. Rev. B 97, 184419 (2018). Copyright 2018 American Physical Society.)

The temperature-dependent magnetic dc susceptibility, specific heat, and neutron-diffraction studies confirm an antiferromagnetic ordering below the Néel temperature ( $T_N$ )  $\sim$  130 K. Neutron-diffraction study reveals an in-plane ( $ab$ -plane)  $120^\circ$  AFM structure [propagation vector  $k = (0\ 0\ 0)$ ] with an ordered moment of  $2.84\ \mu_B/\text{Fe}^{3+}$  at 6 K. Such an AFM ordering is further confirmed by the spin-orbit coupling density functional theory calculations (76). The compound h-LuFeO<sub>3</sub> in its thin-film form shows an additional ferromagnetic component along the crystallographic  $c$  axis along with the in-plane  $120^\circ$  antiferromagnetic ordering (78).

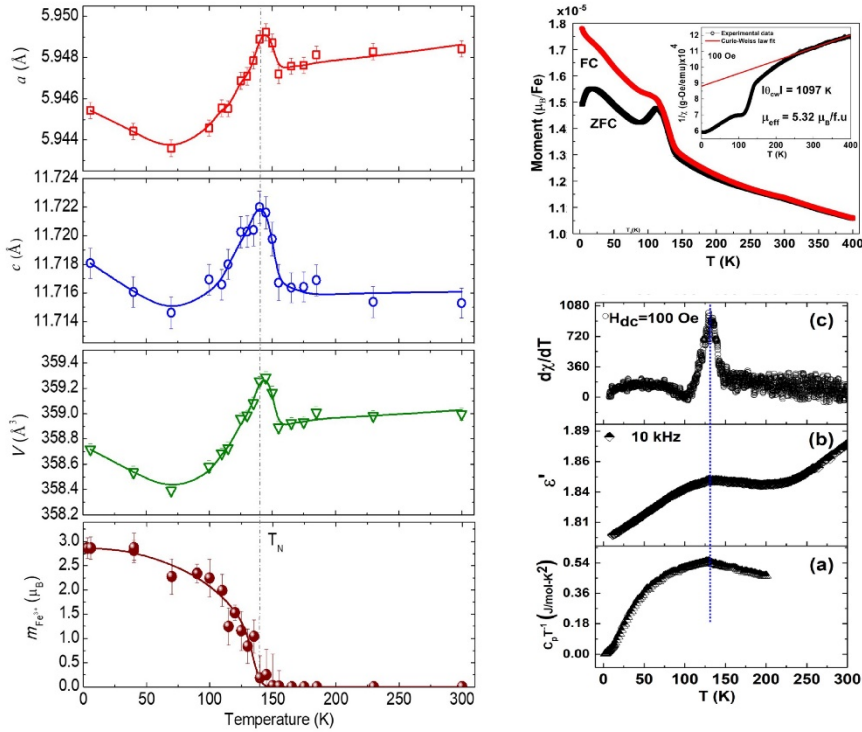


**Figure 28: (left)** Temperature-dependent lattice parameters  $a$ ,  $c$ , the unit-cell volume ( $V$ ), and the ordered magnetic moment of the  $\text{Fe}^{3+}$  ion for  $h\text{-LuFeO}_3$ . **(right)** Temperature-dependent magnetization, heat capacity, dielectric constant, and dc susceptibility curves of bulk  $h\text{-LuFeO}_3$ . (Reprinted with permission from Suresh *et al.* Phys. Rev. B **97**, 184419 (2018). Copyright 2018 American Physical Society.)

A coupling between the lattice, magnetic and electric degrees of freedom is confirmed in the bulk hexagonal  $\text{LuFeO}_3$  (76). An anomaly in the temperature-dependent dielectric curve at the antiferromagnetic ordering temperature  $T_N \sim 130$  K reveals the presence of a magnetoelectric coupling. Furthermore, the anomalies in the lattice constants and unit cell volume at  $T_N$  indicate the presence of a strong magnetoelastic coupling (Fig. 28).

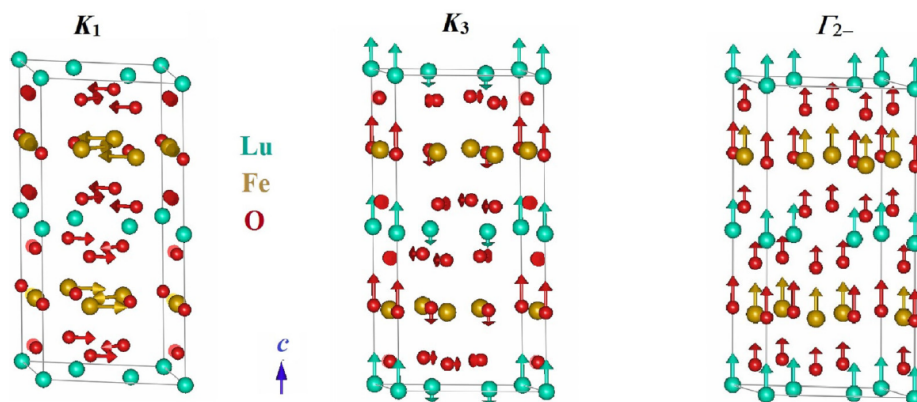


**Figure 29:** The atomic pattern associated with the three phonon modes  $K_1$ ,  $K_3$ , and  $\Gamma_{2-}$ , respectively. (Reprinted with permission from Suresh *et al.* Phys. Rev. B 97, 184419 (2018). Copyright 2018 American Physical Society.)

The structural transition from the non-polar  $P6_3/mmc$  to the polar  $P6_3cm$  phase at the ferroelectric transition temperature  $T_C$  is related to the displacement of atomic positions. These displacements can generally be represented in terms of the  $K_1$ ,  $K_3$ , and  $\Gamma_{2-}$  phonon modes, where,  $K_1$  and  $K_3$  are the zone-boundary modes, and  $\Gamma_{2-}$  is the zone-center polar mode (75) (Fig. 29). In the polar state ( $P6_3cm$  phase), the strong asymmetric covalent bonding interaction between Lu and O along the c axis favors the off-centered electric dipole moment that eventually induces a ferroelectricity (79).

Among the iron-based multiferroics, the  $\text{BiFeO}_3$  with a rhombohedral crystal structure has been investigated extensively and reported to be one of the most promising multiferroic candidates (80, 81). For this compound, both antiferromagnetic (G-type ordering) Néel temperature (approximately 653 K) and ferroelectric Curie temperature are well above the room temperature (approximately 1100 K). Besides, the iron-based family of the multiferroic compounds  $\text{AFeO}_3$  ( $A = \text{Al, Ga, and their mixtures}$ ) possessing a non-centrosymmetric orthorhombic crystal structure shows a coexistence of magnetic and ferroelectric ordering (82, 83). The interesting properties of these compounds appear due to the effect of an anti-site disorder that decides the nature of the magnetic ground state between antiferromagnetic and ferromagnetic, thus controlling the net magnetic moment for a fixed value of the Fe concentration. It is reported that the magnetism induced by the active spin degrees of freedom of Fe cations plays a key role in stabilizing the structure and dynamics of  $\text{GaFeO}_3$ .

## V. Colossal Magnetoresistance and its Tunability in Perovskites

A large change of electrical resistance (conductance) of a compound with the applied magnetic field is known as CMR effect (28, 29). The versatile crystal structure of perovskite  $ABO_3$  materials provides an opportunity to tune the valence state of transition metal in the  $B$  site through a substitution of suitable ions at the  $A$  site which can give rise to the exciting property of CMR. The balance between competing exchange interactions as well as structural and magnetic phases can be effectively tuned via the choice of the trivalent rare-earth ion  $T$  (often  $T = \text{La, Pr, Nd, and Sm}$ ) and the divalent alkali metal ion  $D$  (often  $D = \text{Sr, Ca, and Ba}$ ) elements at the  $A$ -sites of the mixed-valence perovskite manganites  $T_{1-x}D_x\text{MnO}_3$  and their ratio that decides the relative fraction of  $\text{Mn}^{3+}$  and  $\text{Mn}^{4+}$ . In a certain range of the substitution in  $T_{1-x}D_x\text{MnO}_3$  with  $x = 0.2\text{--}0.4$ , the ground state is ferromagnetic, and the paramagnetic-to-ferromagnetic transition is accompanied by the CMR effect (28, 29).

### V.1 Tunable magnetic and electrical properties of $\text{La}_{1-x}\text{Ca}_x\text{MnO}_3$ with substitution

Most of the reported works in the area of CMR perovskites have focused on  $D = \text{Ca}$ - and  $\text{Sr}$ -substituted compounds  $\text{La}_{1-x}D_x\text{MnO}_3$ , and the CMR properties are studied as a function of divalent ion concentration  $x$ . The magnetic and electronic phase diagram and low-temperature behavior of  $\text{La}_{1-x}\text{Ca}_x\text{MnO}_3$  (84, 85) are shown in Fig. 30. The phase boundaries are typically defined by anomalies in the  $M(T)$  data. As shown in Fig. 30 for  $x \leq 0.5$ , there are three distinct phases: the spin-canted insulator, the FM/charge order (CO) insulator, and the FM metal. For  $0.18 < x < 0.5$ , the transition, defined by the anomaly in the  $M(T)$  and  $\rho(T)$  (Fig. 31), shifts to a higher temperature upon application of an external magnetic field. The system undergoes an insulator–metal transition at the FM transition temperature, and a CMR effect is found. For  $x > 0.5$ , there are two distinct phases: CO/CO-AFM insulator and spin-canted insulator. Over the range  $x = 0.5\text{--}0.875$ , the high-temperature phase is defined as a charge-order state. The low-temperature state in this doping regime is an AFM insulator with a transition temperature  $T_N \sim 170 \text{ K}$  (86).

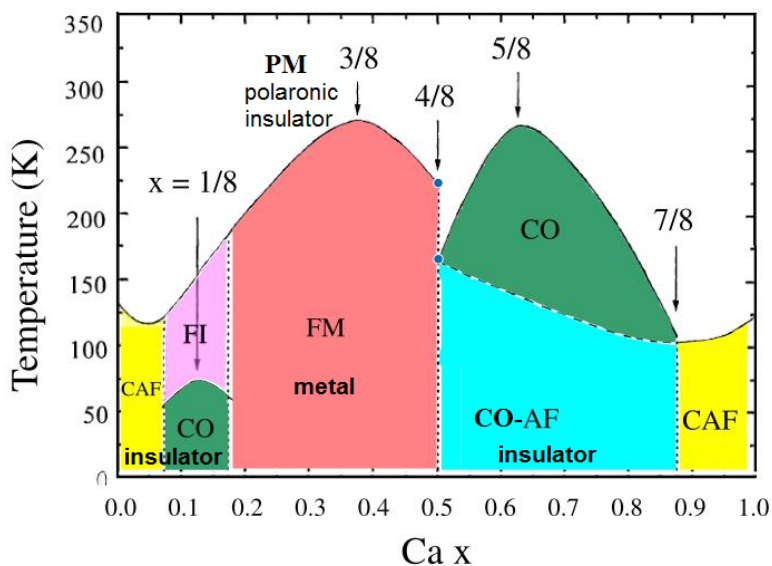


**Figure 30: The magnetic and electronic phase diagrams of the perovskite compound  $\text{La}_{1-x}\text{Ca}_x\text{MnO}_3$ . PM: paramagnetic, CAF: canted antiferromagnet, FI: ferromagnetic insulating, CO: charge-order, FM: ferromagnetic metal.**

Now we discuss the dependence of the CMR behavior (which appears over the substitution range  $x = 0.18-0.5$ ) on the magnetic and structural states. For the concentration  $x = 0.25$ , the temperature-dependent magnetization, resistivity, and magnetoresistance are shown in Fig. 31. The resistivity behaves like a semiconductor,  $d\rho/dT < 0$ , at temperatures above the ferromagnetic Curie point,  $T_c$ . However, below  $T_c$ , there is a sharp reduction in the resistivity along with a transition to a metallic behavior, ( $d\rho/dT > 0$ ). The drop of  $\rho(T)$  into a low-temperature metallic state and the peak in the magnetoresistance (MR) are clearly correlated with the FM transition found in temperature-dependent magnetization data. The MR value is found to be  $\sim 80\%$  under a magnetic field of 4 Tesla. The conduction process appears due to the hopping of magnetic polarons for  $T > T_c$  (87). The carriers are coupled to local FM correlations among the Mn ions, and the conduction occurs through a hopping between spin-aligned  $\text{Mn}^{4+}$  sites. Therefore, such a process is expected to be strongly affected by the lattice effects and disorder and ultimately influences the magnetic and transport properties of these materials. To understand such effects, extensive research works have been done on the metallic-ferromagnetic manganites  $\text{La}_{1-x}\text{Ca}_x\text{MnO}_3$  ( $x=0.3$  and  $0.33$ ), through the substitution of the  $\text{La}^{3+}$  sites with the trivalent rare-earth ions Y, Pr, Dy, Tb, etc of different sizes keeping the fixed Ca concentration (20, 88-93).

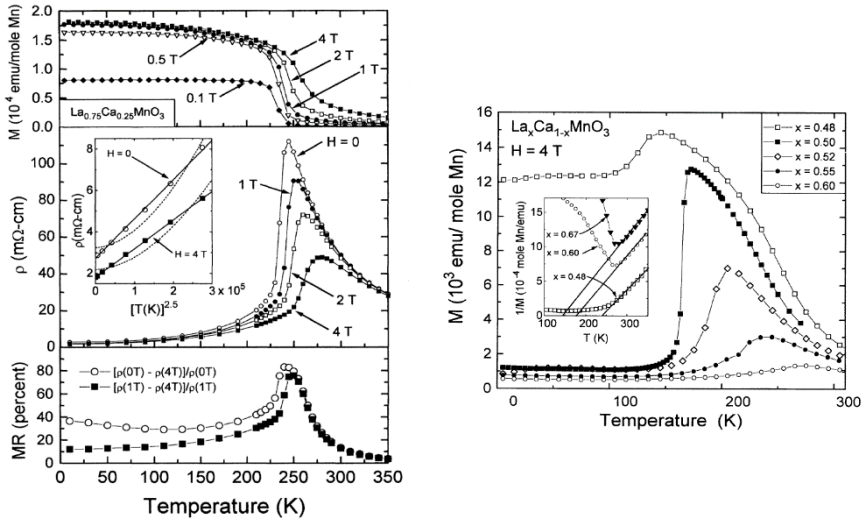


**Figure 31:** (left) The magnetization, resistivity, and magnetoresistance curves for  $\text{La}_{0.75}\text{Ca}_{0.25}\text{MnO}_3$  as a function of temperature at various fields. The inset shows conductivity ( $\rho$ ) curves at low temperatures. (right) The temperature-dependent magnetization curves of  $\text{La}_{1-x}\text{Ca}_x\text{MnO}_3$  at 4 T. The inset shows  $1/M$  vs  $T$  curves with the straight lines correspond to Curie-Weiss fits. Reprinted with permission from Schiffer *et al.* Phys. Rev. Lett. 75 3336 (1995) Copyright 1995 American Physical Society).

The influence of Dy substitution in  $(\text{La}_{1-x}\text{Dy}_x)_{0.7}\text{Ca}_{0.3}\text{MnO}_3$  on the magnetic ordering is shown in Fig. 32 which reveals that the substitution of Dy for La leads to a strong suppression of the magnetic ordering temperature (94-96). The nature of the magnetic state changes from a FM state first to a randomly canted ferromagnetic state (for  $x \sim 0.1$ - 0.3) with a reduced metal-insulator transition temperature, and then to an “insulating” cluster-spin-glass state, and then towards the spin-glass state (for  $x > 0.3$ ) with the increasing Dy substitution (94).

The neutron diffraction results reveal a decrease of the ordered ferromagnetic moment from  $3.42 \pm 0.06$   $m_B/\text{Mn}$  for  $x=0$  to  $3.12 \pm 0.08$   $m_B/\text{Mn}$  for  $x=0.114$ . However, no magnetic Bragg intensities are found for the  $x=0.243$  and  $0.347$  samples down to 15 K confirming the absence of any observable long-range magnetic ordering. Though the bulk dc magnetization data yield a weak spontaneous magnetization ( $=0.17$   $m_B$  per formula unit at 15 K) for the  $x = 0.243$  sample which lies well below the detection limit in the neutron-diffraction experiments. The exact nature of the magnetic states for

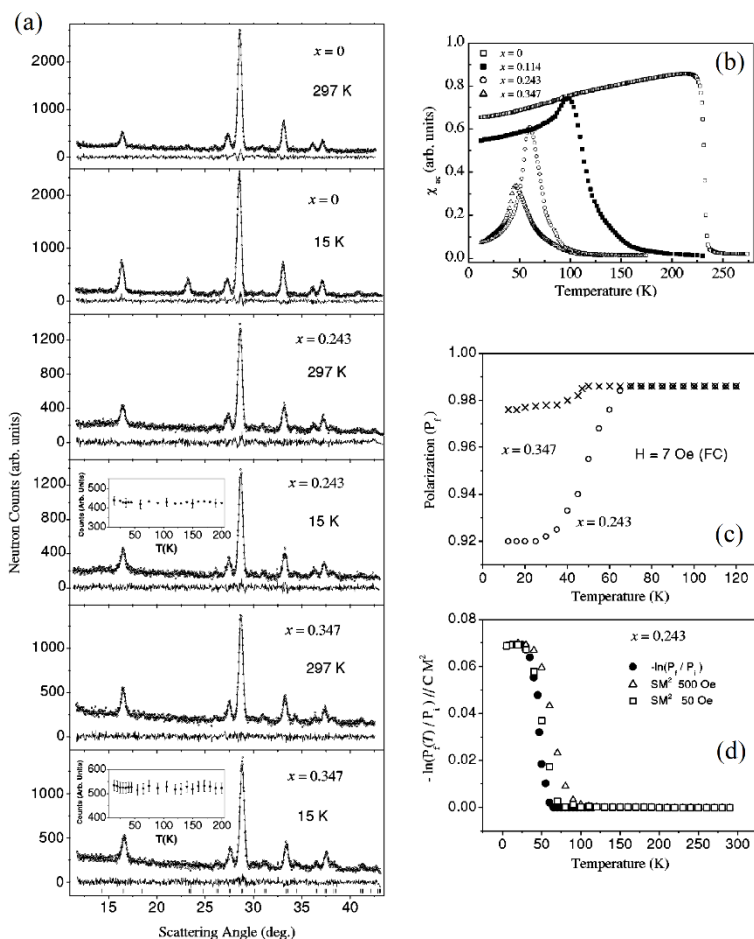


**Figure 32:** (a) Rietveld refined Neutron-diffraction patterns for  $(\text{La}_{1-x}\text{Dy}_x)_{0.7}\text{Ca}_{0.3}\text{MnO}_3$  ( $x = 0, 0.243, \text{ and } 0.347$ ) compounds at  $297\text{ K}$  and  $15\text{ K}$ . The insets show the temperature-dependent combined peak intensity of the (110) and (002) Bragg peaks. (b) The temperature-dependent real part of ac susceptibility. (right-bottom) (c) Temperature-dependent transmitted neutron beam polarization measured under  $7\text{ Oe}$  applied field for the  $x = 0.243$  and  $0.347$  samples. (d) Comparison of  $-\ln[P_i(T)/P_i]$  and  $S[M(T)]^2$  at various fields applied during  $M$  vs  $T$  measurements for the  $x = 0.243$  sample. Reprinted with permission from Yusuf *et al.*, Phys. Rev. B. 68 104421 (2003). Copyright 2003 American Physical Society).

$x = 0.243$  and  $0.347$  samples is determined by neutron depolarization studies (Fig. 32) which reveal  $\sim 7\%$  and  $\sim 1\%$  depolarization of neutron beams for the  $x = 0.243$  and

0.347 samples below their respective magnetic ordering temperatures of  $\sim 65$  and  $47$  K. The ground states are determined to be a metallic-random-canted FM state with a large domain size of  $\sim 5 \mu\text{m}$  and an insulating cluster spin-glass state for  $x=0.243$  and  $0.347$  samples, respectively. The above observations have been attributed to a competition between the coexisting FM double-exchange and the AFM superexchange interactions in the distorted structures with the reduced geometrical tolerance factor  $t$  as well as the randomness [due to random substitutions of smaller  $\text{Dy}^{3+}$  (ionic radius:  $1.083 \text{ \AA}$ ) ions at the  $\text{La}^{3+}$  site (ionic radius:  $1.216 \text{ \AA}$ )].

## V.2 Effect of size reduction on the magnetoresistance and ferromagnetism in $\text{La}_{1-x}\text{Ca}_x\text{MnO}_3$ ( $x \sim 0.33$ )

In section V.1, it has been discussed that the manganite compounds  $\text{La}_{1-x}\text{Ca}_x\text{MnO}_3$  over the substitution range,  $x = 0.2-0.5$  show interesting CMR behavior along with the intrinsic ferromagnetism. In the present section, the effects of the particle size on the magnetoresistance and ferromagnetism are discussed. The reduction of particle size to the nanometer scale has an important role to tune the competing interactions, leading to a different magnetic ground state. Here, we discuss the effects of size reduction on the ferromagnetic nanoparticles of  $\text{La}_{0.67}\text{Ca}_{0.33}\text{MnO}_3$  over a wide particle size range from bulk down to a size of  $15 \text{ nm}$  (97).

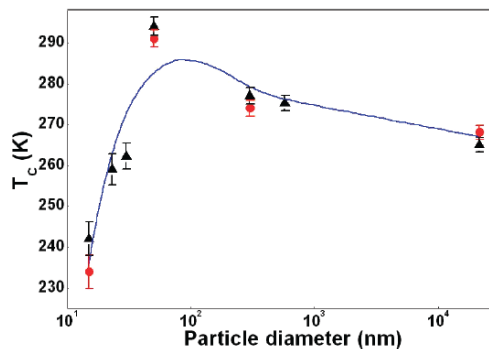


**Figure 33:** The particle size-dependent magnetic ordering temperature  $T_C$  for  $\text{La}_{0.67}\text{Ca}_{0.33}\text{MnO}_3$  nanoparticles. The black triangles and red circles are obtained from magnetization and neutron data, respectively. Reprinted with permission from Sarkar *et al.*, *New Journal of Physics* 12 123026 (2010). Copyright 2010 IOP Publishing Ltd and Deutsche Physikalische Gesellschaft).

The effect of size on the ferromagnetic ordering temperature  $T_c$  is shown in Fig. 33. With the reduction of the particle size ( $d$ ), a non-monotonic variation of the Curie temperature is found. The  $T_c$  value first increases slightly down to  $\sim 50$  nm and then shows a sharp reduction with a further decrease in the particle size. The nature of the  $T_c$  vs  $d$  curve can be well explained by considering two main effects (i) enhancement of the bandwidth ( $W$ ) (dominates in the early stage of size reduction ( $d > 100$  nm)) which enhances the  $T_c$ , and (ii) the finite size effect that tends to decrease the  $T_c$ .

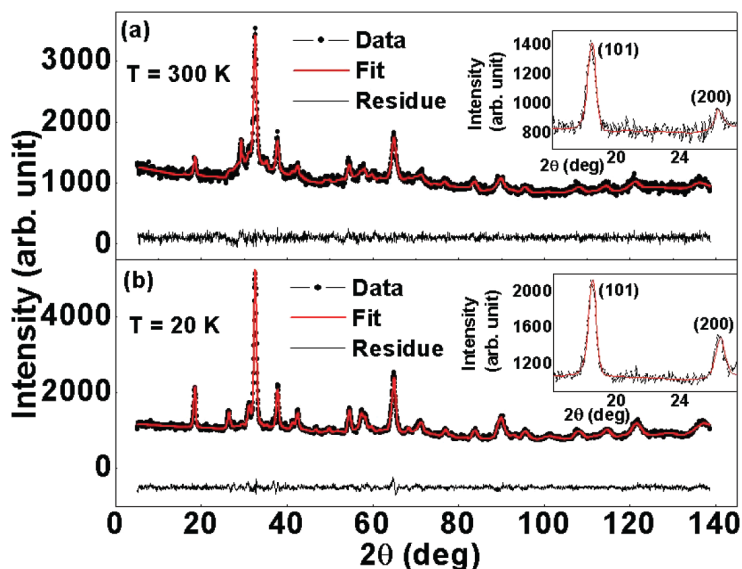


**Figure 34:** The profile fitted neutron diffraction patterns for the  $\text{La}_{0.67}\text{Ca}_{0.33}\text{MnO}_3$  nanoparticles (size 15 nm) measured at (a) 300 and (b) 20 K. The insets show an enlarged view of the diffraction patterns over  $2\theta=16\text{--}30$  deg. Reprinted with permission from Sarkar *et al.*, *New Journal of Physics* 12 123026 (2010). Copyright 2010 IOP Publishing Ltd and Deutsche Physikalische Gesellschaft).

Furthermore, with decreasing particle size, the PM to FM phase transition changes from a first-order to a second-order with the critical exponents approaching the mean-field values (97). This can be explained based on the truncation of the coherence length due to the finite sample size. Neutron diffraction results (Fig. 34) yield that even down to a size of 15 nm the nanoparticles retain ferromagnetic order with a decrease of the spontaneous magnetization ( $M_s$ ) (Fig. 35). The variation of the  $M_s$  with  $d$  is explained based on a core-shell model. The magnetic particles have ordered cores

that can show a long-range ferromagnetic order. The structurally disordered shell (of the thickness  $\delta \sim 2.5$  nm) does not have any spontaneous magnetization and is like a magnetic dead layer. The variation of the  $M_s$  (depicted in Fig. 35) is well accounted by the following relation

$$M_s = M_{oS} \left( 1 - \frac{6\delta}{d} \right) \quad (4)$$

where  $M_{oS}$  is the spontaneous magnetization for a bulk sample that has a long-range magnetic order. The effect of the disordered shell becomes apparent for the smaller diameter particles when  $\delta$  is comparable to  $d$  (the diameter of a particle).

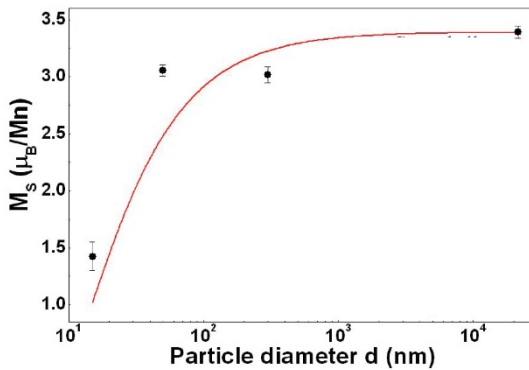


**Figure 35:** The particle size dependence of spontaneous moment for  $\text{La}_{0.67}\text{Ca}_{0.33}\text{MnO}_3$  nanoparticles at  $T = 20$  K. The red line is obtained from the core-shell model using Eq. 5. Reprinted with permission from Sarkar *et al.*, *New Journal of Physics* 12 123026 (2010). Copyright 2010 IOP Publishing Ltd and Deutsche Physikalische Gesellschaft).

Now we discuss the correlation between particle size and magnetotransport in  $\text{La}_{0.67}\text{Ca}_{0.33}\text{MnO}_3$  nanoparticles. As evident from Fig. 36, the ratio of the resistivity  $\rho(T)/\rho(300 \text{ K})$  increases significantly as the particle size decreases. A decrease in the magnetic ordering temperature is also evident with the decrease of the particle size. It is also shown that below a certain particle size ( $\sim 150$  nm) the CMR response disappears (Fig. 36) (98). On the other hand, reducing grain size promotes a rise in tunneling magnetoresistance (Fig. 36), which suppresses the intrinsic response of the material, that is, the CMR peak around the phase transition (98).

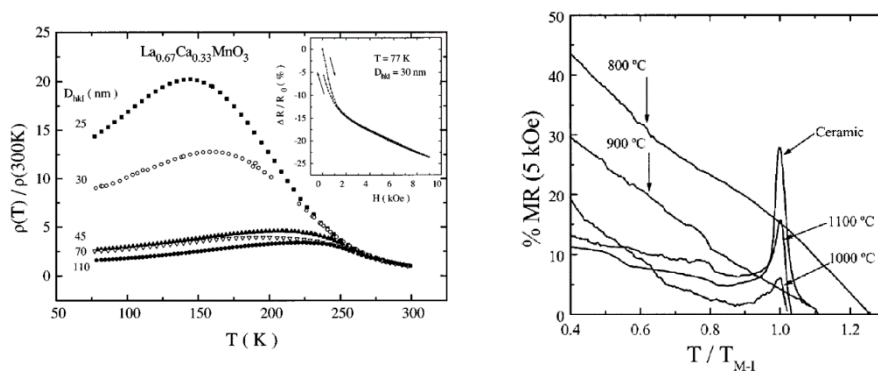


**Figure 36:** (left) The temperature-dependent relative resistivity  $\rho(T)/\rho(300\text{ K})$  of  $\text{La}_{0.67}\text{Ca}_{0.33}\text{MnO}_3$  nanoparticles. Inset shows the magnetoresistance up to 9 kOe at 77 K for the sample with 30 nm size. (right) Magnetoresistance percentage (%MR at a constant field of 5 kOe) vs reduced temperature ( $T/T_{M-I}$ ) curves for the samples with different particle sizes. Reprinted with permission from Sánchez *et al.*, *Appl. Phys. Lett.* 68 134 (1996) and Hueso *et al.*, *J. Appl. Phys.* 86, 3881 (1999), respectively. Copyright 1996 American Institute of Physics).

## VI. Perovskites for Solid Oxide Fuel Cell Applications

The solid oxide fuel cell (SOFC) is an electrochemical conversion device that produces electricity directly from oxidizing a solid fuel and considered to be a green energy source. SOFCs are considered to be suitable for generating electricity because of their simplicity, efficiency, and ability to tolerate some degree of impurities (99). In this regard, the perovskites are one of the most attractive materials for SOFC applications (100) as they have most flexible crystal structures which (i) can host a wide range of ionic radii and valences, and thus exhibiting a high concentration of oxide vacancies and high ionic conductivity, and (ii) has a stable crystal structure over a wide operating temperature range. The schematic construction of the SOFC, composed of an electrolyte layer that is sandwiched between two electrodes (i.e., cathode and anode), is shown in Fig. 37 (101). Two types of conduction i.e., either an oxide ion [Fig. 37(a)] and/or proton [Fig. 37(b)] conduction through the electrolyte can be used in a SOFC device. The electrons generated at the anode (through the oxidation of fuel) are

accepted for oxygen reduction at the cathode. and the electricity is, thus, produced by the flow of electrons in the external circuit (from the anode to the cathode). Since the SOFC uses diffusion of oxide ions (or protons) through a solid electrolyte to obtain current, it is necessary to use high operating temperatures ( $\sim 800\text{--}1000\text{ }^\circ\text{C}$ ) for achieving a high ionic conductivity ( $\sim 0.1\text{ S/cm}$ ) (102). Perovskites can be used as the cathode, anode as well as electrolyte materials in a SOFC device (100).

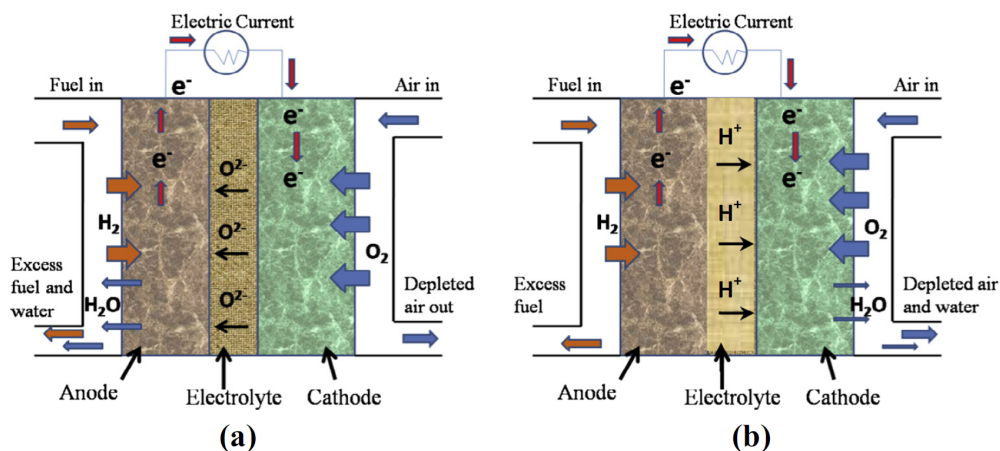


**Figure 37:** Schematic diagrams of solid oxide fuel cells (SOFCs) with (a) oxide-ion conducting electrolyte, and (b) proton-conducting electrolytes. Reprinted with permission from Malavasi *et al.* *Chem. Soc. Rev.* 39, 4370 (2010). Copyright 2010 The Royal Society of Chemistry).

## VI.1 $\text{La}_{1-x}\text{Sr}_x(\text{Mn/Co})\text{O}_{3-\delta}$ perovskites as cathode materials for SOFC

As the SOFCs operate at high temperatures for long periods, a suitable cathode material should have the following properties: (i) high electronic conductivity ( $\sigma > 100\text{ S cm}^{-1}$ ); (ii) high thermal stability and the low thermal expansion coefficient; (iii) chemical compatibility with the electrolyte and interconnect materials; (iv) high catalytic activity for the oxygen reduction reaction; (v) adequate porosity to allow mass transport of oxygen; and (vi) low cost.

The majority of perovskite-type oxides, currently considered as cathodes for SOFC, are based on either the  $\text{La}_{1-x}\text{Sr}_x\text{CoO}_{3-\delta}$  (LSCO) (103, 104) or  $\text{La}_{1-x}\text{Sr}_x\text{MnO}_{3-\delta}$  (LSMO)

materials. LSMO has a high electronic conductivity due to the introduction of  $\text{Sr}^{2+}$  at the  $\text{La}^{3+}$  site which is charge-compensated by the Mn ( $\text{Mn}^{3+}$ – $\text{Mn}^{4+}$ ), making it a good cathode material at high temperatures ( $> 1000\text{ }^\circ\text{C}$ ). However, it does not work well as a cathode at intermediate temperatures ( $500\text{ }^\circ\text{C}$ – $700\text{ }^\circ\text{C}$ ) (105). The oxygen vacancy in LSMO is strongly influenced by the Sr content. Over the Sr concentration range ( $x=0$ – $0.5$ ), all the compounds of LSMO have the rhombohedral crystal symmetry (Space group:  $R\bar{3}c$ ) (Fig. 38) (106). The lattice parameter  $a_h$  initially increases up to  $x = 0.1$ , and then shows a linear decrease with the substitution of  $\text{Sr}^{2+}$  (106). Similar behavior is found for the angle  $\alpha_r$ . On the other hand, the lattice constant  $c_h$  remains unchanged with the substitution of  $\text{Sr}^{2+}$ . The decrease of the lattice parameters  $a_h$  and  $\alpha_r$  with the substitution is due to the increase of the ratio of  $\text{Mn}^{4+}$  (ionic size:  $0.53\text{ \AA}$ ) and  $\text{Mn}^{3+}$  (ionic size:  $0.645\text{ \AA}$ ).

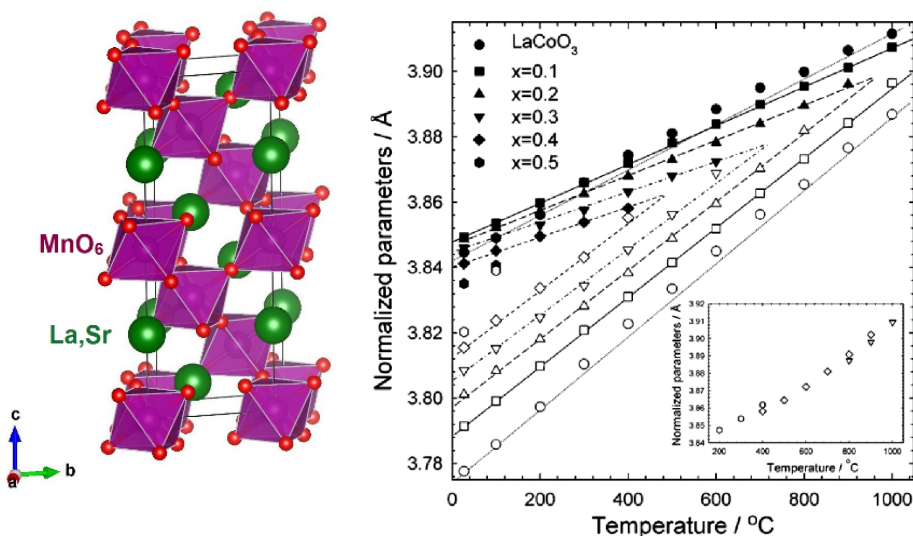


**Figure 38:** (left) The rhombohedral crystal structure of the perovskite compound  $\text{La}_{1-x}\text{Sr}_x\text{MnO}_{3-\delta}$ . (right) The temperature variation of the normalized hexagonal lattice parameters of  $\text{La}_{1-x}\text{Sr}_x\text{CoO}_3$ . The lines are linear fits to the data. The inset shows the temperature variation of the cubic lattice parameters for the  $x = 0.3$  compound. Reprinted with permission from Mastine *et al.* Chem. Mater. 18, 6047 (2006). Copyright 2006 American Chemical Society).

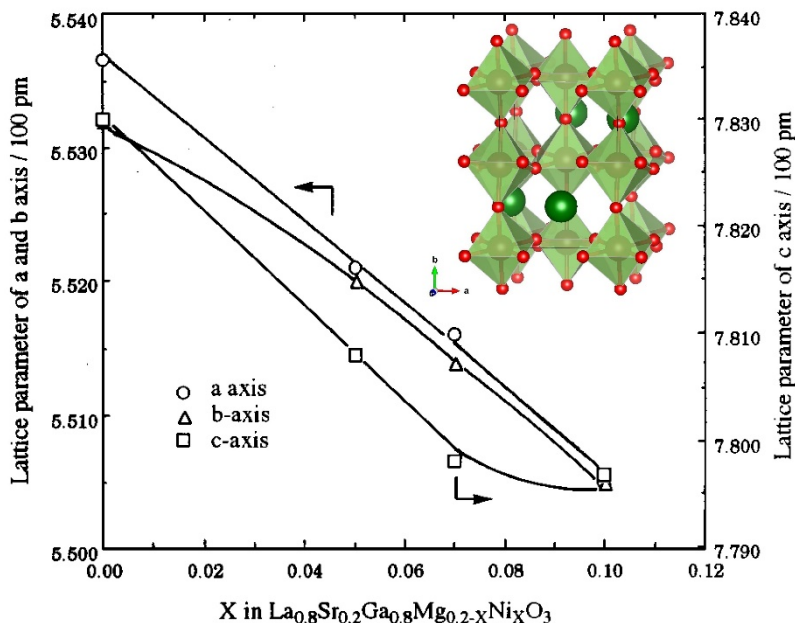


**Figure 39:** The variation of lattice parameters as a function of Ni concentration in  $\text{La}_{0.8}\text{Sr}_{0.2}\text{Ga}_{0.8}\text{Mg}_{0.2-x}\text{Ni}_x\text{O}_3$ . The inset shows the orthorhombic crystal structure of  $\text{La}_{0.8}\text{Sr}_{0.2}\text{Ga}_{0.8}\text{Mg}_{0.2-x}\text{Ni}_x\text{O}_3$ . Reprinted with permission from Ishihara *et al.*, *J. Mater. Sci.* 36 1125 (2001). Copyright 2001 Kluwer Academic Publishers).

Furthermore, the greater charge density of the  $\text{Mn}^{4+}$  cation favors the contraction of the Mn-O bonds hence the contraction of the unit cell. The unchanged values of the  $c_h$  with substitution could be understood on the basis of a counter compensation by the larger  $\text{Sr}^{2+}$  ionic radius (1.44 Å) as compared to that for the  $\text{La}^{3+}$  ion (1.36 Å). We note that  $\text{Sr}^{2+}/\text{La}^{3+}$  ions are located along the z-axis of the hexagonal unit cell (106). The replacement of La with other rare-earth ions shows promising results where  $\text{Pr}_{0.7}\text{Sr}_{0.3}\text{MnO}_{3-\delta}$  ( $\sigma = 226$  S/cm at 500°C) and  $\text{Nd}_{0.7}\text{Sr}_{0.3}\text{MnO}_3$  are found to be most suitable cathode materials in terms of thermal expansion coefficient, reactivity, and conductivity (107). The use of calcium (instead of Sr) as a dopant in the lanthanide site can offer promising results as well, as in the case of  $\text{Pr}_{0.7}\text{Ca}_{0.3}\text{MnO}_{3-\delta}$ , which does not react with the electrolyte and has a maximum conductivity of 266  $\text{S cm}^{-1}$  (108).

An alternative to the manganite perovskites LSMO, the lanthanum cobaltite

perovskites doped with bivalent metals, such as Ca or Sr ( $\text{La}_{1-x}(\text{Sr/Ca})_x\text{MnO}_{3-\delta}$ ) also exhibit high conductivity values for  $x = 0.3 - 0.4$ . The compounds  $\text{La}_{1-x}\text{Sr}_x\text{CoO}_{3-\delta}$  also have a rhombohedral crystal structure with the space group  $R-3c$  at an ambient temperature. With increasing temperature, the rhombohedral distortion from the cubic symmetry decreased nearly linearly up to the phase transition to the cubic perovskite structure (Fig. 38). The phase transition temperature decreases rapidly with increasing Sr content in  $\text{La}_{1-x}\text{Sr}_x\text{CoO}_{3-\delta}$  (109). However, their high thermal expansion coefficient ( $\sim 2-3$  times higher than that for their Mn counterpart) is the main limitation for their application (109).

## VI.2 Perovskites as anode materials of SOFC

The requirements for a SOFC anode material are high ionic and electronic conductivity over a wide oxygen partial pressure ( $p\text{O}_2$ ) range, and surface oxygen exchange kinetics and good catalytic properties. The most widely studied perovskites for the SOFC anode material are the titanates and chromites. The  $\text{SrTiO}_3$ -type titanates have received a great deal of attention as anode materials for SOFC due to their high stability under a reducing atmosphere at high temperatures (110). The poor conductivity of this material can be overcome through the introduction of an appropriate substitution in the crystal structure (111). With yttrium substitution at the A-site of  $\text{SrTiO}_3$ , the electrical conductivity of  $\text{SrTiO}_3$  reaches a significant value  $\sim 100 \text{ S cm}^{-1}$  (112). The substituted  $\text{LaCrO}_3$ -based materials are mainly used as interconnects in high-temperature SOFCs and are stable in reducing environments. The B-site (Cr-site) of  $\text{La}_{1-x}\text{Sr}_x\text{CrO}_3$  has been substituted with various transition metals (Mn, Fe, Co, Ni, and Cu) to introduce oxygen vacancies (113). Recently,  $\text{AMoO}_3$  perovskites ( $A = \text{Ca, Sr, and Ba}$ ), containing  $\text{Mo}^{4+}$  ions have also received interest for their potential use as anodes with high electrical conductivity ( $\sim 10^4 \text{ S cm}^{-1}$ ) (114). The limitation of oxide ions diffusion can be overcome through the substitution of other metals, such as Fe, Cr, or Co at the Mo site (115).

## VI.3 Perovskite-based electrolytes in SOFC

The electrolyte of a fuel cell is responsible for (i) ion conduction between the electrodes, (ii) the blocking of internal electronic conduction (i.e., forcing the electrons to flow through the external circuit), and (iii) the separation of the reacting gases. Electrolytes can be grouped based on the conducting species, i.e., oxygen ion conductors and proton conductors. The criteria for the electrolyte materials are (i)

structural stability in both reducing and oxidizing environments, and (ii) high ionic conductivity but low electronic conductivity at the SOFC operating temperature (116). The lanthanum gallate perovskite compounds  $\text{La}_{1-x}\text{Sr}_x\text{Ga}_{1-y}\text{Mg}_y\text{O}_{3-d}$  (LSGM) show a high oxygen ion conductivity (117). Furthermore, a substitution of a small amount of Ni at the B-site of LSGM is reported to improve the performance without introducing an electronic conductivity (118) (Fig. 39). However, due to the high activation energy for oxygen ion conduction (Fig. 40), the performance of SOFC with oxygen-ion conducting electrolyte decreases sharply with decreasing temperature. The proton conductor based SOFC devices (119) can operate at lower temperatures over 350 – 600 °C. Among the perovskite oxides,  $\text{BaCeO}_3$  –based materials are regarded as the benchmark materials for the high and nearly pure proton conductivity (120). The chemical stability of  $\text{BaCeO}_3$  against  $\text{CO}_2$ ,  $\text{SO}_2$ , and  $\text{H}_2\text{O}$  can be solved by a partial replacement of  $\text{Ce}^{4+}$  by  $\text{Zr}^{4+}$  and  $\text{Yb}^{3+}$  (121).

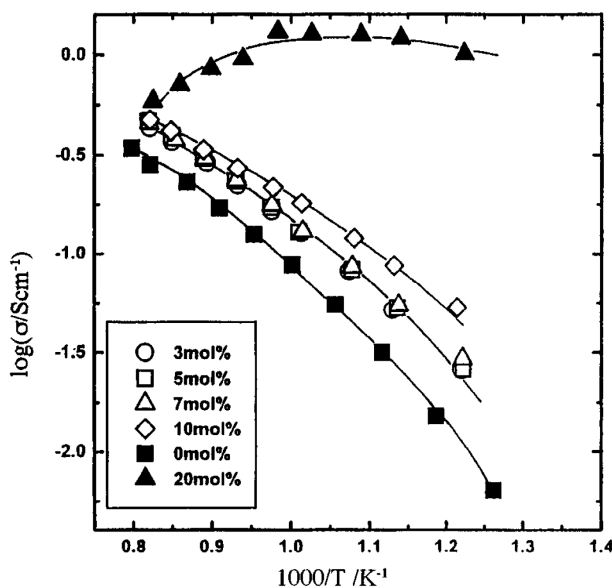


**Figure 40:** Arrhenius plots of the electrical conductivity of  $\text{La}_{0.8}\text{Sr}_{0.2}\text{Ga}_{0.8}\text{Mg}_{0.2-x}\text{Ni}_x\text{O}_3$ . Reprinted with permission from Ishihara et al., *J. Mater. Sci.* 36 1125 (2001). Copyright 2001 Kluwer Academic Publishers).

## VII. Future Prospective of Perovskites

The perovskites have been serving fertile playgrounds for the realization of numerous fundamental concepts of physics, chemistry, and material science over the last century. The interest in perovskites is ever-growing as there are new discoveries from time to time in this area. The perovskites have also been utilized in various practical devices due to their superior properties. We discuss below a few of upcoming research fields in the area of perovskite.

### VII.1 Perovskites based photovoltaic solar cells

Perovskites have recently attracted a considerable attention as potential solar-cell materials because of their low cost, flexibility, and relatively easy manufacturing process (122).

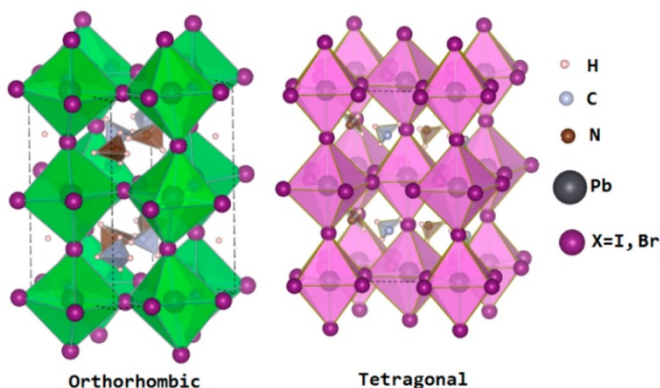


**Figure 41:** The crystal structures of tetragonal and orthorhombic  $\text{CH}_3\text{NH}_3\text{PbX}_3$  ( $X = \text{I}$  and  $\text{Br}$ ) phases. The rigid framework consisting of the  $\text{PbX}_6$  octahedral is also highlighted in the structure. Reprinted with permission from Feng *et al.*, *J. Phys. Chem. Lett.* 5, 1278 (2014). Copyright 2014 American Chemical Society.

Especially, the organolead halide perovskite materials having an organic cation (e.g., methylammonium  $\text{CH}_3\text{NH}_3^+$ , ethyl-ammonium  $\text{CH}_3\text{CH}_2\text{NH}_3^+$ , formamidinium  $\text{NH}_2\text{CH}=\text{NH}_2^+$ ), a metal cation of the carbon family (i.e.,  $\text{Ge}^{2+}$ ,  $\text{Sn}^{2+}$ ,  $\text{Pb}^{2+}$ ), and a halogen anion (i.e.,  $\text{F}^-$ ,  $\text{Cl}^-$ ,  $\text{Br}^-$ ,  $\text{I}^-$ ) are used in solar-cell. A high absorption coefficient, long charge carrier diffusion length, low-temperature processing, and

ambipolar behavior of these materials are suitable for the low-cost solar cells. Therefore, the perovskite materials can be used as a light-absorbing layer, as well as an electron/hole transport layer. Recently a record power conversion efficiency (PCE) of about 23 percent has been achieved based on the perovskite material (123) which is significant as the theoretical limit of maximum efficiency is about 31 percent. However, the perovskite solar cells still have great barriers to further improvements and commercial production. The biggest problem comes with the natural instability of perovskite materials, especially the most widely-used methylammonium lead iodide ( $\text{MAPbI}_3$ ) (Fig. 41). The crystal structural phase transition within the range of solar cell operation temperature is a problem for device applications. The crystal structural instability with varying temperature and pressure over the operating temperature range is the present challenge and an open research topic. The second challenge is to develop a non-toxic replacement of the lead (Pb) based perovskite materials. Solving the above issues on the perovskite solar cells would form the leading research topics in the coming years.

## VII.2 Hybrid perovskites with metal-organic frameworks

Hybrid inorganic-organic or metal-organic frameworks (MOFs), consisting of metal ions linked together by organic bridging ligands, are recently-identified crystalline materials and form a new development in the area of materials science. These materials benefit from the characteristics of both inorganic and organic building blocks; and possess new and interesting properties/functionalities. In particular, the MOFs with the perovskite-like crystal structure  $\text{ABX}_3$  (Fig. 42) are of special interest as the wide possible selection of  $A$  and  $B$  provides plenty of options for adjusting their magnetic and electric properties. For example, perovskite-type  $\text{ABX}_3$  MOFs with  $A$  = guanidinium  $[\text{C}(\text{NH}_2)_3]^+$  (124, 125), or ammonium  $\text{NH}_4$  (126), or methylammonium formate  $[\text{CH}_3\text{NH}_3]$  (127) or niccolite-like  $[\text{NH}_2(\text{CH}_3)_2]$  (128),  $B$  = transition metal ions, and  $X$  = formates ( $\text{HCOO}^-$ ) show multiferroic behavior. Magnetism is also one of the major areas of interest in MOFs due to the flexibility to tune/control the nature of the magnetic couplings through a careful choice of the building blocks, metal ions, short ligands, co-ligands, and templates. MOFs are promising candidates to realize low-dimensional magnetic topology and to investigate the quantum magnetic phenomena. The perovskite-type MOFs, therefore, appear to be the new promising materials in the coming days.

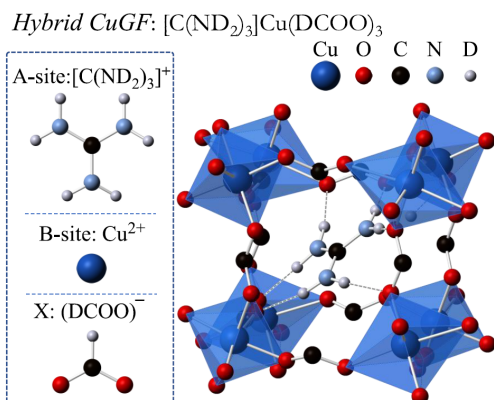


**Figure 42:** Crystal structure of the metal-organic framework compound  $[\text{C}(\text{ND}_2)_3]\text{Cu}^{2+}(\text{DCOO})_3$  with the perovskite structure. The  $\text{CuO}_6$  octahedra (shaded octahedra) linked via formates replicating the  $\text{ABX}_3$  topology. For clarity, the formate-D atoms are not shown. Reprinted with permission from Viswanathan *et al.*, *J. Phys. Chem. C*, **123**, 18551 (2019). Copyright 2019 American Chemical Society).

### VII.3 Crystal structural engineering of perovskites

Recent studies show that the crystal structure of the perovskites, especially the coordination of the transition metal oxide at the *B* site could be engineered by a proper chemical reaction (129). This provides a new way to tune the electronic and magnetic properties of perovskites. By low-temperature topochemical reaction using the calcium hydride as a reductant, unique iron oxides with square-planar coordination have been prepared (Fig. 43). It is shown that the  $\text{Fe}(\text{II})\text{O}_4$  square-planar geometry is more strongly bonded than any known  $\text{Fe}(\text{II})$  oxide and exhibits a spin transition in  $\text{Fe}(\text{II})$  in a four-coordinated metal bonding. Research on such crystal structural engineering is expected to gear up in the near future and would be of a new research direction in perovskites.

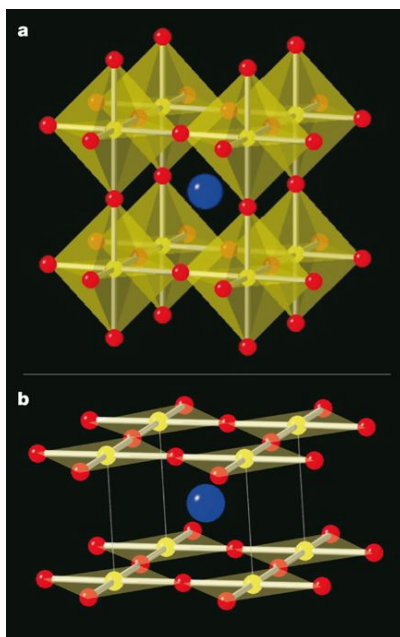


**Figure 43:** (a) The cubic perovskite crystal structure of SrFeO<sub>3</sub>. (b) The crystal structure of the infinite-layer compound SrFeO<sub>2</sub>. Iron, strontium, and oxygen atoms are represented as yellow, blue, and red spheres, respectively. The octahedral and square planer coordinations of iron ions are shown by shades in (a) and (b), respectively. Reprinted with permission from Tsujimoto *et al.*, Nature 450, 1062 (2007). Copyright 2007 Nature Publishing Group).

## VII.4 Mixed anion perovskites

Presently, inorganic compounds including perovskites are mostly based on single anion, such as oxide or chloride or bromide or iodide. The compounds with multiple anions beyond the single-oxide/halide ion, such as oxyhalides and oxyhydrides, offer a new materials-platform with superior functionality (130). The structures and physical properties of most mixed-anions are less explored with much to learn. The local structure of these compounds, where the metal cation is bonded to more than one anionic ligand to form a heteroleptic polyhedron, leads to new properties. The different anionic characteristics, such as charge, ionic radii, electronegativity, and polarizability add new dimensions to control and tune the electronic and atomic structure of materials, lead to the phenomena those are not accessible in a single-anion analogue. In this regard, perovskites could provide a

strong platform to realize the multi-anion compounds and discover new properties. Recently such possibilities are shown for few perovskites viz.,  $\text{SrMO}_2\text{N}$  ( $M = \text{Nb, Ta}$ ),  $\text{LaTaON}_2$  (131),  $\text{AVO}_2\text{N}$  ( $A = \text{Pr, Nd}$ ) (132), and  $\text{BaTiO}_3\text{-xHx}$  (133). The study of mixed anion perovskites is expected to be one of the leading research areas in the coming years.

## VIII. Conclusion

---

Perovskite oxides show their ability to have a wide range of physical properties, as well as applications in numerous advanced devices. The versatility of the perovskite in regards to its flexible crystal structure and its ability to incorporate many modifying cations leads to a series of novel properties. The possibility of tailoring composition, chemical, structural, and physical properties allows one to think that their future will be as important as their splendid past. Some of the physical properties of perovskites, and their correlations to the underlined crystal structure have been discussed in this chapter. In particular, various aspects of magnetic, multiferroic, magnetotransport, and ionic properties have been covered.

The perovskite materials have already shown their potential for applications in various fields. The future aims of perovskite materials are toward the technological improvements to enhance their applications. The strong advances in nanotechnologies along with the development of new multiferroics, heterostructures, and photovoltaic open some of the most promising horizons for researches in the field of materials science based on perovskite-type structures. In addition to the conventional perovskites, the hybrid metal-organic framework perovskites and mixed anion perovskites would be of the future for smart materials for novel properties.

### Acknowledgments:

We sincerely acknowledge the contributions of all the coauthors of our published articles on the perovskite materials.

**Complementary informations on authors:**

e-mail, ORCID, Research Gate, LinkedIn profiles, etc

**A. K. Bera**

[akbera@barc.gov.in](mailto:akbera@barc.gov.in)

ORCID: 0000-0003-0222-0990

Research Gate: [www.researchgate.net/profile/Anup\\_Kumar\\_Bera](http://www.researchgate.net/profile/Anup_Kumar_Bera)

Researcher id: K-6477-2015

**S. M. Yusuf**

[smyusuf@barc.gov.in](mailto:smyusuf@barc.gov.in)

ORCID: 0000-0003-1898-4610

Research Gate: [www.researchgate.net/profile/S\\_Yusuf2/](http://www.researchgate.net/profile/S_Yusuf2/)

Researcher id:

**Cite this paper:** A.K. Bera and S. M. Yusuf, OAJ Materials and Devices, vol 5(1), Chap No 2 in "Perovskites and other Framework Structure Crystalline Materials", p39 (Coll. Acad. 2021)  
DOI:10.23647/ca.md20202105

**REFERENCES**

1. Goldshmidt VM. Geochemische verteilungsgesetze der elemente VII. die gesetze der krystallochemie. Norske Videnskaps - Akademi, Matemtsik - Naturvidenskapelig Klasse I, Skifter, Oslo,. 1926: 2.
2. Yusuf SM, Kumar A. Neutron scattering of advanced magnetic materials. Applied Physics Reviews. 2017;4(3):031303.
3. Howard CJ, Stokes HT. Group-Theoretical Analysis of Octahedral Tilting in Perovskites. Acta Crystallographica Section B. 1998;54(6):782-9.
4. Mitchell RH, Welch MD, Chakhmouradian AR. Nomenclature of the perovskite supergroup: A hierarchical system of classification based on crystal structure and composition. Mineralogical Magazine. 2018;81(3):411-61.

5. Nasir M, Khan M, Bhatt S, Bera AK, Furquan M, Kumar S, *et al.* Influence of Cation Order and Valence States on Magnetic Ordering in  $\text{La}_2\text{Ni}_{1-x}\text{Mn}_{1+x}\text{O}_6$ . *Physica Status Solidi (b)*. 2019;0(0):1900019.
6. Manna K, Bera AK, Jain M, Elizabeth S, Yusuf SM, Anil Kumar PS. Structural-modulation-driven spin canting and reentrant glassy magnetic phase in ferromagnetic  $\text{Lu}_2\text{MnNiO}_6$ . *Physical Review B*. 2015;91(22):224420.
7. Manna K, Sarkar R, Fuchs S, Onykieenko YA, Bera AK, Cansever GA, *et al.* Noncollinear antiferromagnetism of coupled spins and pseudospins in the double perovskite  $\text{La}_2\text{CuIrO}_6$ . *Physical Review B*. 2016;94(14):144437.
8. Rao CNR. Transition Metal Oxides. *Annual Review of Physical Chemistry*. 1989;40(1):291-326.
9. Rao CNR, Seikh MM, Narayana C. Spin-State Transition in  $\text{LaCoO}_3$  and Related Materials. In: Gütllich P, Goodwin HA, editors. *Spin Crossover in Transition Metal Compounds II*. Berlin, Heidelberg: Springer Berlin Heidelberg; 2004. p. 1-21.
10. Tokura Y, Nagaosa N. Orbital Physics in Transition-Metal Oxides. *Science*. 2000;288(5465):462.
11. Anderson PW. Exchange in Insulators: Superexchange, Direct Exchange, and Double Exchange. In: Rado GT, Suhl H, editors. *Magnetism*: Academic Press; 1963. p. 25-83.
12. Zener C. Interaction Between the  $d$  Shells in the Transition Metals. *Physical Review*. 1951;81(3):440-4.
13. Zener C. Interaction between the  $d$ -Shells in the Transition Metals. II. Ferromagnetic Compounds of Manganese with Perovskite Structure. *Physical Review*. 1951;82(3):403-5.
14. Dzyaloshinskii I. Theory of helical structures in antiferromagnets I: Nonmetals. *Sov Phys JETP*. 1964;19:960-71.
15. Moriya T. Anisotropic Superexchange Interaction and Weak Ferromagnetism. *Physical Review*. 1960;120(1):91-8.
16. Kimura T, Goto T, Shintani H, Ishizaka K, Arima T, Tokura Y. Magnetic control of ferroelectric polarization. *Nature*. 2003;426(6962):55-8.
17. Sarkar P, Mandal P, Bera AK, Yusuf SM, Sharath Chandra LS, Ganesan V. Field-induced first-order to second-order magnetic phase transition in  $\text{Sm}_{0.52}\text{Sr}_{0.48}\text{MnO}_3$ . *Physical Review B*. 2008;78(1):012415.
18. Sarkar P, Mandal P, Mydeen K, Bera AK, Yusuf SM, Arumugam S, *et al.* Role of external and internal perturbations on the ferromagnetic phase transition in  $\text{Sm}_{0.52}\text{Sr}_{0.48}\text{MnO}_3$ . *Physical Review B*. 2009;79(14):144431.
19. De Teresa JM, Ritter C, Algarabel PA, Yusuf SM, Blasco J, Kumar A, *et al.* Detailed neutron study of the crossover from long-range to short-range magnetic

- ordering in  $(\text{Nd}_{1-x}\text{Tb}_x)_{0.55}\text{Sr}_{0.45}\text{MnO}_3$  manganites. *Physical Review B*. 2006;74(22):224442.
20. Yusuf SM, De Teresa JM, Ritter C, Serrate D, Ibarra MR, Yakhmi JV, *et al.* Possible quantum critical point in  $(\text{La}_{1-x}\text{Dy}_x)_{0.7}\text{Ca}_{0.3}\text{MnO}_3$ . *Physical Review B*. 2006;74(14):144427.
21. Manna PK, Yusuf SM. Two interface effects: Exchange bias and magnetic proximity. *Physics Reports*. 2014;535(2):61-99.
22. Manna PK, Yusuf SM, Mukadam MD, Kohlbrecher J. Evidence of a core-shell structure in the antiferromagnetic  $\text{La}_{0.2}\text{Ce}_{0.8}\text{CrO}_3$  nanoparticles by neutron scattering. *Applied Physics A*. 2012;109(2):385-90.
23. Manna PK, Yusuf SM, Shukla R, Tyagi AK. Coexistence of sign reversal of both magnetization and exchange bias field in the core-shell type  $\text{La}_{0.2}\text{Ce}_{0.8}\text{CrO}_3$  nanoparticles. *Applied Physics Letters*. 2010;96(24):242508.
24. Liu H, Yang X. A brief review on perovskite multiferroics. *Ferroelectrics*. 2017;507(1):69-85.
25. Wang J, Neaton JB, Zheng H, Nagarajan V, Ogale SB, Liu B, *et al.* Epitaxial  $\text{BiFeO}_3$ ; Multiferroic Thin Film Heterostructures. *Science*. 2003;299(5613):1719.
26. Khomskii D. Classifying multiferroics: Mechanisms and effects. *Physics Reports*. 2009;2 20.
27. Wang KF, Liu JM, Ren ZF. Multiferroicity: the coupling between magnetic and polarization orders. *Advances in Physics*. 2009;58(4):321-448.
28. Ramirez AP. Colossal magnetoresistance. *Journal of Physics: Condensed Matter*. 1997;9(39):8171-99.
29. Rao CNR, Cheetham AK, Mahesh R. Giant Magnetoresistance and Related Properties of Rare-Earth Manganates and Other Oxide Systems. *Chemistry of Materials*. 1996;8(10):2421-32.
30. Dagotto E, Hotta T, Moreo A. Colossal magnetoresistant materials: the key role of phase separation. *Physics Reports*. 2001;344(1):1-153.
31. Rao CNR, Raychaudhuri AK. Colossal magnetoresistance, charge ordering and other novel properties of manganates and related materials. *Colossal Magnetoresistance, Charge Ordering and Related Properties of Manganese Oxides: World Scientific*; 1998. p. 1-42.
32. Millis AJ, Shraiman BI, Mueller R. Dynamic Jahn-Teller Effect and Colossal Magnetoresistance in  $\text{La}_{1-x}\text{Sr}_x\text{MnO}_3$ . *Physical Review Letters*. 1996;77(1):175-8.
33. Razavi FS, Gross G, Habermeier HU, Lebedev O, Amelinckx S, Van Tendeloo G, *et al.* Epitaxial strain induced metal insulator transition in  $\text{La}_{0.9}\text{Sr}_{0.1}\text{MnO}_3$  and  $\text{La}_{0.88}\text{Sr}_{0.1}\text{MnO}_3$  thin films. *Applied Physics Letters*. 2000;76(2):155-7.

34. Choi KJ, Biegalski M, Li YL, Sharan A, Schubert J, Uecker R, *et al.* Enhancement of Ferroelectricity in Strained BaTiO<sub>3</sub> Thin Films. *Science*. 2004;306(5698):1005.
35. Ohtomo A, Muller DA, Grazul JL, Hwang HY. Artificial charge-modulation in atomic-scale perovskite titanate superlattices. *Nature*. 2002;419(6905):378-80.
36. Fan M, Zhang W, Jian J, Huang J, Wang H. Strong perpendicular exchange bias in epitaxial La<sub>0.7</sub>Sr<sub>0.3</sub>MnO<sub>3</sub>:LaFeO<sub>3</sub> nanocomposite thin films. *APL Materials*. 2016;4(7):076105.
37. Nedelcu G, Protesescu L, Yakunin S, Bodnarchuk MI, Grotevent MJ, Kovalenko MV. Fast Anion-Exchange in Highly Luminescent Nanocrystals of Cesium Lead Halide Perovskites (CsPbX<sub>3</sub>, X = Cl, Br, I). *Nano Letters*. 2015;15(8):5635-40.
38. Skinner SJ. Recent advances in Perovskite-type materials for solid oxide fuel cell cathodes. *International Journal of Inorganic Materials*. 2001;3(2):113-21.
39. Larramendi IRd, Ortiz-Vitoriano I, Saen N, Dzul-Bautista B, Rojo T. Designing Perovskite Oxides for Solid Oxide Fuel Cells. In: Pan L, Zhu G, editors. *Perovskite Materials - Synthesis, Characterisation, Properties, and Applications*: IntechOpen February 3rd 2016.
40. Service RF. Perovskite LEDs begin to shine. *Science*. 2019;364(6444):918.
41. Yang Y, Dai H, Yang F, Zhang Y, Luo D, Zhang X, *et al.* All-Perovskite Photodetector with Fast Response. *Nanoscale Research Letters*. 2019;14(1):291.
42. Yu W, Li F, Yu L, Niazi MR, Zou Y, Corzo D, *et al.* Single crystal hybrid perovskite field-effect transistors. *Nature Communications*. 2018;9(1):5354.
43. Atta NF, Galal A, El-Ads EH. Perovskite Nanomaterials - Synthesis, Characterization, and Applications. In: Zhu LPaG, editor. *Perovskite Materials - Synthesis, Characterisation, Properties, and Applications*: IntechOpen; February 3rd 2016.
44. Kanamori J. Superexchange interaction and symmetry properties of electron orbitals. *Journal of Physics and Chemistry of Solids*. 1959;10(2):87-98.
45. Kanamori J. Crystal Distortion in Magnetic Compounds. *Journal of Applied Physics*. 1960;31(5):S14-S23.
46. Kugel KI, Khomskii DI. The Jahn-Teller effect and magnetism: transition metal compounds. *Soviet Physics Uspekhi*. 1982;25(4):231-56.
47. Viswanathan M, Anil Kumar PS, Bhadram VS, Narayana C, Bera AK, Yusuf SM. Influence of lattice distortion on the Curie temperature and spin-phonon coupling in LaMn<sub>0.5</sub>Co<sub>0.5</sub>O<sub>3</sub>. *Journal of Physics: Condensed Matter*. 2010;22(34):346006.
48. Joy PA, Kholam YB, Date SK. Spin states of Mn and Co in LaMn<sub>0.5</sub>Co<sub>0.5</sub>O<sub>3</sub>. *Physical Review B*. 2000;62(13):8608-10.

49. Chen L, Yuan C, Xue J, Wang J. B-site ordering and magnetic behaviours in Ni-doped double perovskite  $\text{Sr}_2\text{FeMoO}_6$ . *Journal of Physics D: Applied Physics*. 2005;38(22):4003-8.
50. Woodward P, Hoffmann RD, Sleight AW. Order-disorder in  $\text{A}_2\text{M}^{3+}\text{M}^{5+}\text{O}_6$  perovskites. *Journal of Materials Research*. 2011;9(8):2118-27.
51. Balcells L, Navarro J, Bibes M, Roig A, Martínez B, Fontcuberta J. Cationic ordering control of magnetization in  $\text{Sr}_2\text{FeMoO}_6$  double perovskite. *Applied Physics Letters*. 2001;78(6):781-3.
52. Chakraborty KR, Das A, Yusuf SM, Krishna PSR, Tyagi AK. Low-temperature neutron diffraction study of  $\text{La}_{1-x}\text{Nd}_x\text{CrO}_3$  ( $x=0.05, 0.1, 0.2$  and  $0.25$ ). *Journal of Magnetism and Magnetic Materials*. 2006;301(1):74-8.
53. Chakraborty KR, Yusuf SM, Tyagi AK. Magnetic ordering in  $\text{La}_{0.75}\text{Sr}_{0.25}\text{CrO}_3$ : A neutron diffraction study. *Journal of Magnetism and Magnetic Materials*. 2008;320(6):1163-6.
54. Chakraborty KR, Mukherjee S, Kaushik SD, Rayaprol S, Prajapat CL, Singh MR, *et al.* Low temperature neutron diffraction study of  $\text{Nd}_{1-x}\text{Sr}_x\text{CrO}_3$  ( $0.05 \leq x \leq 0.15$ ). *Journal of Magnetism and Magnetic Materials*. 2014;361:81-7.
55. Shukla R, Manjanna J, Bera AK, Yusuf SM, Tyagi AK.  $\text{La}_{1-x}\text{Ce}_x\text{CrO}_3$  ( $0.0 \leq x \leq 1.0$ ): A New Series of Solid Solutions with Tunable Magnetic and Optical Properties. *Inorganic Chemistry*. 2009;48(24):11691-6.
56. Shukla R, Bera AK, Yusuf SM, Deshpande SK, Tyagi AK, Hermes W, *et al.* Multifunctional Nanocrystalline  $\text{CeCrO}_3$ : Antiferromagnetic, Relaxor, and Optical Properties. *The Journal of Physical Chemistry C*. 2009;113(29):12663-8.
57. Yoshii K, Nakamura A, Ishii Y, Morii Y. Magnetic Properties of  $\text{La}_{1-x}\text{Pr}_x\text{CrO}_3$ . *Journal of Solid State Chemistry*. 2001;162(1):84-9.
58. Hemberger J, Lobina S, Krug von Nidda HA, Tristan N, Ivanov VY, Mukhin AA, *et al.* Complex interplay of  $3d$  and  $4f$  magnetism in  $\text{La}_{1-x}\text{Gd}_x\text{MnO}_3$ . *Physical Review B*. 2004;70(2):024414.
59. Kumar A, Yusuf SM, Ritter C. Nd-ordering-driven Mn spin reorientation and magnetization reversal in the magnetostructurally coupled compound  $\text{NdMnO}_3$ . *Physical Review B*. 2017;96(1):014427.
60. Kumar A, Yusuf SM. The phenomenon of negative magnetization and its implications. *Physics Reports*. 2015:1-34.
61. Halasyamani PS, Poepelmeier KR. Noncentrosymmetric Oxides. *Chemistry of Materials*. 1998;10(10):2753-69.
62. von Hippel A. Ferroelectricity, Domain Structure, and Phase Transitions of Barium Titanate. *Reviews of Modern Physics*. 1950;22(3):221-37.

63. Anderson PW. Antiferromagnetism. Theory of Superexchange Interaction. *Physical Review*. 1950;79(2):350-6.
64. Goodenough JB. Theory of the Role of Covalence in the Perovskite-Type Manganites  $[La, M^{II}]MnO_3$ . *Physical Review*. 1955;100(2):564-73.
65. Tachibana M, Shimoyama T, Kawaji H, Atake T, Takayama-Muromachi E. Jahn-Teller distortion and magnetic transitions in perovskite  $RMnO_3$  ( $R=Ho, Er, Tm, Yb, \text{ and } Lu$ ). *Physical Review B*. 2007;75(14):144425.
66. Lorenz B. Hexagonal Manganites  $RMnO_3$ : Class (I) Multiferroics with Strong Coupling of Magnetism and Ferroelectricity. *ISRN Condensed Matter Physics*. 2013;2013:43.
67. Van Aken BB, Palstra TTM, Filippetti A, Spaldin NA. The origin of ferroelectricity in magnetoelectric  $YMnO_3$ . *Nature Materials*. 2004;3(3):164-70.
68. Fiebig M, Lottermoser T, Pisarev RV. Spin-rotation phenomena and magnetic phase diagrams of hexagonal  $RMnO_3$ . *Journal of Applied Physics*. 2003;93(10):8194-6.
69. Cheong S-W, Mostovoy M. Multiferroics: a magnetic twist for ferroelectricity. *Nature Materials*. 2007;6(1):13-20.
70. Chakraborty KR, Paul B, Shukla R, Krishna PSR, Kumar A, Mukadam MD, *et al.* Revealing magnetic ordering and spin-phonon coupling in  $Y_{1-x}Tb_xMnO_3$  ( $0.1 \leq x \leq 0.3$ ) compounds. *Journal of Physics: Condensed Matter*. 2017;29(15):155804.
71. Chakraborty KR, Shukla R, Kaushik SD, Mukadam MD, Siruguri V, Tyagi AK, *et al.* Tuning of magnetic ordering by Y substitution onto Tb site in the nanocrystalline  $TbMnO_3$ . *Journal of Applied Physics*. 2015;118(16):164307.
72. Bossak AA, Graboy IE, Gorbenko OY, Kaul AR, Kartavtseva MS, Svetchnikov VL, *et al.* XRD and HREM Studies of Epitaxially Stabilized Hexagonal Orthoferrites  $RFeO_3$  ( $R = Eu-Lu$ ). *Chemistry of Materials*. 2004;16(9):1751-5.
73. Shang M, Zhang C, Zhang T, Yuan L, Ge L, Yuan H, *et al.* The multiferroic perovskite  $YFeO_3$ . *Applied Physics Letters*. 2013;102(6):062903.
74. Akbashev AR, Semisalova AS, Perov NS, Kaul AR. Weak ferromagnetism in hexagonal orthoferrites  $RFeO_3$  ( $R = Lu, Er-Tb$ ). *Applied Physics Letters*. 2011;99(12):122502.
75. Das H, Wysocki AL, Geng Y, Wu W, Fennie CJ. Bulk magnetoelectricity in the hexagonal manganites and ferrites. *Nature Communications*. 2014;5:2998.
76. Suresh P, Vijaya Laxmi K, Bera AK, Yusuf SM, Chittari BL, Jung J, *et al.* Magnetic ground state of the multiferroic hexagonal  $LuFeO_3$ . *Physical Review B*. 2018;97(18):184419.
77. Wang W, Zhao J, Wang W, Gai Z, Balke N, Chi M, *et al.* Room-Temperature Multiferroic Hexagonal  $LuFeO_3$  Films. *Physical Review Letters*. 2013;110(23):237601.

78. Disseler SM, Borchers JA, Brooks CM, Mundy JA, Moyer JA, Hillsberry DA, *et al.* Magnetic Structure and Ordering of Multiferroic Hexagonal LuFeO<sub>3</sub>. *Physical Review Letters*. 2015;114(21):217602.
79. Jeong YK, Lee J-H, Ahn S-J, Jang HM. Epitaxially Constrained Hexagonal Ferroelectricity and Canted Triangular Spin Order in LuFeO<sub>3</sub> Thin Films. *Chemistry of Materials*. 2012;24(13):2426-8.
80. Dutta DP, Mandal BP, Mukadam MD, Yusuf SM, Tyagi AK. Improved magnetic and ferroelectric properties of Sc and Ti codoped multiferroic nano BiFeO<sub>3</sub> prepared via sonochemical synthesis. *Dalton Transactions*. 2014;43(21):7838-46.
81. Mukherjee A, Basu S, Manna PK, Yusuf SM, Pal M. Enhancement of multiferroic properties of nanocrystalline BiFeO<sub>3</sub> powder by Gd-doping. *Journal of Alloys and Compounds*. 2014;598:142-50.
82. Saha R, Shireen A, Bera AK, Shirodkar SN, Sundarayya Y, Kalarikkal N, *et al.* Structure and magnetic properties of the Al<sub>1-x</sub>Ga<sub>x</sub>FeO<sub>3</sub> family of oxides: A combined experimental and theoretical study. *Journal of Solid State Chemistry*. 2011;184(3):494-501.
83. Saha R, Shireen A, Shirodkar SN, Waghmare UV, Sundaresan A, Rao CNR. Multiferroic and magnetoelectric nature of GaFeO<sub>3</sub>, AlFeO<sub>3</sub> and related oxides. *Solid State Communications*. 2012;152(21):1964-8.
84. Schiffer P, Ramirez AP, Bao W, Cheong SW. Low Temperature Magnetoresistance and the Magnetic Phase Diagram of La<sub>1-x</sub>Ca<sub>x</sub>MnO<sub>3</sub>. *Physical Review Letters*. 1995;75(18):3336-9.
85. Mahesh R, Mahendiran R, Raychaudhuri AK, Rao CNR. Giant Magnetoresistance in Bulk Samples of La<sub>1-x</sub>A<sub>x</sub>MnO<sub>3</sub> (A = Sr or Ca). *Journal of Solid State Chemistry*. 1995;114(1):297-9.
86. Ramirez AP, Schiffer P, Cheong SW, Chen CH, Bao W, Palstra TTM, *et al.* Thermodynamic and Electron Diffraction Signatures of Charge and Spin Ordering in La<sub>1-x</sub>Ca<sub>x</sub>MnO<sub>3</sub>. *Physical Review Letters*. 1996;76(17):3188-91.
87. von Helmolt R, Wecker J, Holzapfel B, Schultz L, Samwer K. Giant negative magnetoresistance in perovskitelike La<sub>2/3</sub>Ba<sub>1/3</sub>MnO<sub>x</sub> ferromagnetic films. *Physical Review Letters*. 1993;71(14):2331-3.
88. Yusuf SM, Sahana M, Hegde MS, Dörr K, Müller KH. Evidence of ferromagnetic domains in the La<sub>0.67</sub>Ca<sub>0.33</sub>Mn<sub>0.9</sub>Fe<sub>0.1</sub>O<sub>3</sub> perovskite. *Physical Review B*. 2000;62(2):1118-23.
89. Yusuf SM, Ganguly R, Chakraborty KR, Mishra PK, Paranjpe SK, Yakhmi JV, *et al.* Effect of Dy substitution for La in La<sub>0.7</sub>Ca<sub>0.3</sub>MnO<sub>3</sub> perovskite. *Journal of Alloys and Compounds*. 2001;326(1):89-93.

90. Yusuf SM, Sahana M, Dörr K, Röblier UK, Müller KH. Effect of Ga doping for Mn on the magnetic properties of  $\text{La}_{0.67}\text{Ca}_{0.33}\text{MnO}_3$ . *Physical Review B*. 2002;66(6):064414.
91. Yusuf SM, Chakraborty KR, Ganguly R, Mishra PK, Paranjpe SK, Yakhmi JV, *et al.* Evidence of ferromagnetic domains in the  $(\text{La}_{0.757}\text{Dy}_{0.243})_{0.7}\text{Ca}_{0.3}\text{MnO}_3$  perovskite. *Journal of Magnetism and Magnetic Materials*. 2004;272-276:1288-9.
92. Röblier S, Röblier UK, Nenkov K, Eckert D, Yusuf SM, Dörr K, *et al.* Rounding of a first-order magnetic phase transition in Ga-doped  $\text{La}_{0.67}\text{Ca}_{0.33}\text{MnO}_3$ . *Physical Review B*. 2004;70(10):104417.
93. Yusuf SM, De Teresa JM, Algarabel PA, Blasco J, Ibarra MR, Kumar A, *et al.* Nature of the magnetic ordering for small mean-size and large-size mismatch of A-site cations in CMR manganites. *Physica B: Condensed Matter*. 2006;385-386:401-4.
94. Yusuf SM, Chakraborty KR, Paranjpe SK, Ganguly R, Mishra PK, Yakhmi JV, *et al.* Magnetic and electrical properties of  $(\text{La}_{1-x}\text{Dy}_x)_{0.7}\text{Ca}_{0.3}\text{MnO}_3$  perovskites. *Physical Review B*. 2003;68(10):104421.
95. Mahesh R, Mahendiran R, Raychaudhuri AK, Rao CNR. Effect of particle size on the giant magnetoresistance of  $\text{La}_{0.7}\text{Ca}_{0.3}\text{MnO}_3$ . *Applied Physics Letters*. 1996;68(16):2291-3.
96. Gayathri N, Raychaudhuri AK, Tiwary SK, Gundakaram R, Arulraj A, Rao CNR. Electrical transport, magnetism, and magnetoresistance in ferromagnetic oxides with mixed exchange interactions: A study of the  $\text{La}_{0.7}\text{Ca}_{0.3}\text{Mn}_{1-x}\text{Co}_x\text{O}_3$  system. *Physical Review B*. 1997;56(3):1345-53.
97. Sarkar T, Raychaudhuri AK, Bera AK, Yusuf SM. Effect of size reduction on the ferromagnetism of the manganite  $\text{La}_{1-x}\text{Ca}_x\text{MnO}_3$  ( $x=0.33$ ). *New Journal of Physics*. 2010;12(12):123026.
98. Hueso LE, Sande P, Miguéns DR, Rivas J, Rivadulla F, López-Quintela MA. Tuning of the magnetocaloric effect in  $\text{La}_{0.67}\text{Ca}_{0.33}\text{MnO}_{3-\delta}$  nanoparticles synthesized by sol-gel techniques. *Journal of Applied Physics*. 2002;91(12):9943-7.
99. Mahato N, Banerjee A, Gupta A, Omar S, Balani K. Progress in material selection for solid oxide fuel cell technology: A review. *Progress in Materials Science*. 2015;72:141-337.
100. Sunarso J, Hashim SS, Zhu N, Zhou W. Perovskite oxides applications in high temperature oxygen separation, solid oxide fuel cell and membrane reactor: A review. *Progress in Energy and Combustion Science*. 2017;61:57-77.
101. Malavasi L, Fisher CAJ, Islam MS. Oxide-ion and proton conducting electrolyte materials for clean energy applications: structural and mechanistic features. *Chemical Society Reviews*. 2010;39(11):4370-87.
102. Steele BCH, Heinzel A. Materials for fuel-cell technologies. *Nature*. 2001;414(6861):345-52.

103. Chakraborty KR, Yusuf SM, Krishna PSR, Ramanadham M, Tyagi AK, Pomjakushin V. Structural study of  $\text{La}_{0.75}\text{Sr}_{0.25}\text{CrO}_3$  at high temperatures. *Journal of Physics: Condensed Matter*. 2006;18(37):8661-72.
104. Chakraborty KR, Yusuf SM, Krishna PSR, Ramanadham M, Pomjakushin V, Tyagi AK. Structural stability of orthorhombic and rhombohedral  $\text{La}_{0.75}\text{Nd}_{0.25}\text{CrO}_3$ : a high-temperature neutron diffraction study. *Journal of Physics: Condensed Matter*. 2007;19(21):216207.
105. Jacobson AJ. Materials for Solid Oxide Fuel Cells. *Chemistry of Materials*. 2010;22(3):660-74.
106. Hammouche A, Siebert E, Hammou A. Crystallographic, thermal and electrochemical properties of the system  $\text{La}_{1-x}\text{Sr}_x\text{MnO}_3$  for high temperature solid electrolyte fuel cells. *Materials Research Bulletin*. 1989;24(3):367-80.
107. Sakaki Y, Takeda Y, Kato A, Imanishi N, Yamamoto O, Hattori M, *et al.*  $\text{Ln}_{1-x}\text{Sr}_x\text{MnO}_3$  ( $\text{Ln}=\text{Pr, Nd, Sm}$  and  $\text{Gd}$ ) as the cathode material for solid oxide fuel cells. *Solid State Ionics*. 1999;118(3):187-94.
108. Rim H-R, Jeung S-K, Jung E, Lee J-S. Characteristics of  $\text{Pr}_{1-x}\text{M}_x\text{MnO}_3$  ( $\text{M} = \text{Ca, Sr}$ ) as cathode material in solid oxide fuel cells. *Materials Chemistry and Physics*. 1998;52(1):54-9.
109. Mastin J, Einarsrud M-A, Grande T. Structural and Thermal Properties of  $\text{La}_{1-x}\text{Sr}_x\text{CoO}_{3-\delta}$ . *Chemistry of Materials*. 2006;18(25):6047-53.
110. Verbraeken MC, Ramos T, Agersted K, Ma Q, Savaniu CD, Sudireddy BR, *et al.* Modified strontium titanates: from defect chemistry to SOFC anodes. *RSC Advances*. 2015;5(2):1168-80.
111. Yurkiv V, Constantin G, Hornes A, Gondolini A, Mercadelli E, Sanson A, *et al.* Towards understanding surface chemistry and electrochemistry of  $\text{La}_{0.1}\text{Sr}_{0.9}\text{TiO}_{3-\alpha}$  based solid oxide fuel cell anodes. *Journal of Power Sources*. 2015;287:58-67.
112. Hui S, Petric A. Electrical Properties of Yttrium-Doped Strontium Titanate under Reducing Conditions. *Journal of The Electrochemical Society*. 2002;149(1):J1-J10.
113. Tao S, Irvine JTS. A redox-stable efficient anode for solid-oxide fuel cells. *Nature Materials*. 2003;2(5):320-3.
114. Chamberland BL, Danielson PS. Alkaline-earth vanadium (IV) oxides having the  $\text{AVO}_3$  composition. *Journal of Solid State Chemistry*. 1971;3(2):243-7.
115. Martínez-Coronado R, Alonso JA, Aguadero A, Fernández-Díaz MT. Optimized energy conversion efficiency in solid-oxide fuel cells implementing  $\text{SrMo}_{1-x}\text{Fe}_x\text{O}_{3-\delta}$  perovskites as anodes. *Journal of Power Sources*. 2012;208:153-8.
116. Medvedev DA, Lyagaeva JG, Gorbova EV, Demin AK, Tsiakaras P. Advanced materials for SOFC application: Strategies for the development of highly conductive

- and stable solid oxide proton electrolytes. *Progress in Materials Science*. 2016;75:38-79.
117. Ishihara T, Matsuda H, Takita Y. Doped LaGaO<sub>3</sub> Perovskite Type Oxide as a New Oxide Ionic Conductor. *Journal of the American Chemical Society*. 1994;116(9):3801-3.
118. Ishihara T, Shibayama T, Nishiguchi H, Takita Y. Oxide ion conductivity in La<sub>0.8</sub>Sr<sub>0.2</sub>Ga<sub>0.8</sub>Mg<sub>0.2-x</sub>Ni<sub>x</sub>O<sub>3</sub> perovskite oxide and application for the electrolyte of solid oxide fuel cells. *Journal of Materials Science*. 2001;36(5):1125-31.
119. Zhu Z, Sun W, Shi Z, Liu W. Proton-conducting solid oxide fuel cells with yttrium-doped barium zirconate electrolyte films sintered at reduced temperatures. *Journal of Alloys and Compounds*. 2016;658:716-20.
120. Iwahara H, Uchida H, Ono K, Ogaki K. Proton Conduction in Sintered Oxides Based on BaCeO<sub>3</sub>. *Journal of The Electrochemical Society*. 1988;135(2):529-33.
121. Zuo C, Zha S, Liu M, Hatano M, Uchiyama M. Ba(Zr<sub>0.1</sub>Ce<sub>0.7</sub>Y<sub>0.2</sub>)O<sub>3-δ</sub> as an Electrolyte for Low-Temperature Solid-Oxide Fuel Cells. *Advanced Materials*. 2006;18(24):3318-20.
122. Dong Q, Fang Y, Shao Y, Mulligan P, Qiu J, Cao L, *et al.* Electron-hole diffusion lengths >175 μm in solution-grown CH<sub>3</sub>NH<sub>3</sub>PbI<sub>3</sub> single crystals. *Science*. 2015;347(6225):967.
123. Li X, Bi D, Yi C, Décoppet J-D, Luo J, Zakeeruddin SM, *et al.* A vacuum flash-assisted solution process for high-efficiency large-area perovskite solar cells. *Science*. 2016;353(6294):58.
124. Hu K-L, Kurmoo M, Wang Z, Gao S. Metal–Organic Perovskites: Synthesis, Structures, and Magnetic Properties of [C(NH<sub>2</sub>)<sub>3</sub>][M<sup>II</sup>(HCOO)<sub>3</sub>] (M=Mn, Fe, Co, Ni, Cu, and Zn; C(NH<sub>2</sub>)<sub>3</sub>= Guanidinium). *Chemistry – A European Journal*. 2009;15(44):12050-64.
125. Viswanathan M, Bhat SG, Bera AK, Rodríguez-Carvajal J. Neutron Diffraction Study on the Magnetic Structure of the Promised Multiferroic Hybrid Perovskite [C(ND<sub>2</sub>)<sub>3</sub>]Cu(DCOO)<sub>3</sub> and Its Centrosymmetric Analogues. *The Journal of Physical Chemistry C*. 2019;123(30):18551-9.
126. Lawler JMM, Manuel P, Thompson AL, Saines PJ. Probing ferroic transitions in a multiferroic framework family: a neutron diffraction study of the ammonium transition metal formates. *Dalton Transactions*. 2015;44(25):11613-20.
127. Gómez-Aguirre LC, Pato-Doldán B, Mira J, Castro-García S, Señarís-Rodríguez MA, Sánchez-Andújar M, *et al.* Magnetic Ordering-Induced Multiferroic Behavior in [CH<sub>3</sub>NH<sub>3</sub>][Co(HCOO)<sub>3</sub>] Metal–Organic Framework. *Journal of the American Chemical Society*. 2016;138(4):1122-5.

128. Zhao J-P, Xu J, Han S-D, Wang Q-L, Bu X-H. A Niccolite Structural Multiferroic Metal–Organic Framework Possessing Four Different Types of Bistability in Response to Dielectric and Magnetic Modulation. *Advanced Materials*. 2017;29(23):1606966.
129. Tsujimoto Y, Tassel C, Hayashi N, Watanabe T, Kageyama H, Yoshimura K, *et al.* Infinite-layer iron oxide with a square-planar coordination. *Nature*. 2007;450:1062.
130. Kageyama H, Hayashi K, Maeda K, Attfield JP, Hiroi Z, Rondinelli JM, *et al.* Expanding frontiers in materials chemistry and physics with multiple anions. *Nature Communications*. 2018;9(1):772.
131. Clark L, Oró-Solé J, Knight KS, Fuertes A, Attfield JP. Thermally Robust Anion-Chain Order in Oxynitride Perovskites. *Chemistry of Materials*. 2013;25(24):5004-11.
132. Oró-Solé J, Clark L, Bonin W, Attfield JP, Fuertes A. Anion-ordered chains in a d1 perovskite oxynitride: NdVO<sub>2</sub>N. *Chemical Communications*. 2013;49(24):2430-2.
133. Yajima T, Takeiri F, Aidzu K, Akamatsu H, Fujita K, Yoshimune W, *et al.* A labile hydride strategy for the synthesis of heavily nitridized BaTiO<sub>3</sub>. *Nature Chemistry*. 2015;7:1017.